AIR-GROUND CHANNEL MODELING AND WAVEFORM CONTAINMENT

A THESIS SUBMITTED TO
THE GRADUATE SCHOOL OF
ENGINEERING AND NATURAL SCIENCES
OF ISTANBUL MEDIPOL UNIVERSITY
IN PARTIAL FULFILLMENT OF THE REQUIREMENTS FOR
THE DEGREE OF
MASTER OF SCIENCE
IN
ELECTRICAL, ELECTRONICS ENGINEERING AND CYBER SYSTEMS

By
Mostafa Ibrahim
March, 2017

ABSTRACT

AIR-GROUND CHANNEL MODELING AND WAVEFORM CONTAINMENT

Mostafa Ibrahim
M.S. in Electrical, Electronics Engineering and Cyber Systems
Advisor: Prof. Dr. Hüseyin Arslan
March, 2017

The content of this work is divided into two main parts. Part I is dedicated for characterizing Air-Ground channels. Applications using Air-Ground communications are expected to grow in the future. Low altitude phases of these wireless links are considered severe channels, as they experience huge delay and Doppler spreads, however, they are not yet accurately characterized in the literature. Chapter 1 presents an analytic three-dimensional Air-Ground Doppler-delay spread spectrum model for dense scattering environments. In Chapter 2, a numerical terrain based Doppler-delay spread model simulator was proposed. It was demonstrated that the terrain topography affects the shape of the Doppler-delay spread spectrum. The scattering function becomes unique for each terrain and position of the ground station and air station.

In Part II, waveform design and containment techniques are discussed. A scheme called Zero tail Filter Bank Spread Orthogonal Frequency Division Multiplexing (ZT FB-S-OFDM) is proposed in Chapter 3. In this scheme, Raised cosine (RC) pulses coexist in the same signal, with an abrupt transition of roll-off factors α at edges of the stream. The pulses near the edges are RC pulses with $\alpha = 1$ and the ones in between have the value $\alpha = 0$. In Chapter 4, the possibility of using the same scheme but with a smooth roll-off factors transition is introduced. This is proposed along with the time-frequency space warping principle to preserve the orthogonality between the pulses. Simulations show high containment gains for both of the proposed schemes.

Keywords: Air-ground, Doppler, doubly dispersve, DFT-S-OFDM, Filter Bank, warping, nonuniform sampling .

ÖZET

HAVA-YER KANAL MODELLEMESİ VE DALGA FORMU YERLEŞTİRME

Mostafa Ibrahim
Elektrik-Elektronik Mühendisliği ve Siber Sistemler, Yüksek Lisans
Tez Danışmanı: Prof. Dr. Hüseyin Arslan
Mart, 2017

Elektrik-Elektronik Mühendisliği ve Siber Sistemler, Yüksek Lisans

Bu çalışma iki ana kısımdan oluşmaktadır. Birinci kısım Hava-Yer kanallarının karakterize edilmesine ayrılmıştır. İkinci kısım ise, dalga formu tasarım ve sınırlandırma teknikleri için ayrılmıştır. Gelecekte, Hava-Yer haberleşmesini kullanan uygulamaların artması beklenmektedir. Yüksek zaman ve frekans (Doppler) saçılması sebebiyle, bu tür kablosuz linklerin düşük irtifa fazı etkili kanallar olarak kabul edilmektedir. Ancak, literatürde bu tür kanalların karakterizasyonuna dair net bir çalışma bulunmamaktadır. Birinci bölümde, analitik üç boyutlu gecikme/Doppler yayılı spectrum modeli yoğun saçılımlı ortamlar için sunulmuştur. İkinci bölümde ise numerik bölge tabanlı bir Doppler/gecikme yayılım modeli simülatörü önerilmiştir. Bu şekilde, bölge topografisinin gecikme/Doppler yayılı spectrumunun şeklini etkilediği gösterilmiştir. Ayrıca saçılma fonksiyonu, yer ve hava istasyonunun pozisyonu ve bölgesine mahsus değerler almaktadır.

İkinci kısımda, dalga formu tasarımı ve sınırlandırma teknikleri tartışılmıştır. Bu bağlamda üçüncü bölümde "Zero tail Filter Bank Spread Orthogonal Frequency Division Multiplexing (ZT FB-s-OFDM)" olarak adlandırılan yeni bir yöntem önerilmiştir. Bu yöntemde, Raised cosine (RC) darbeleri kenarlarda ani devrilme faktörü α geçişleri ile birlikte aynı sinyal içinde yer almaktadır. Kenarlardaki darbeler $\alpha = 1$ değerine sahipken, ortalarda yer alanlar $\alpha = 0$ değeri almaktadır. Dördüncü bölümde, aynı yöntem devrilme faktörü değerlerinde yumuşak bir geçiş ile önerilmiştir. Bu yöntem, darbeler arasındaki ortogonalliği korumak için zaman-frekans-uzay dolama prensibi ile birlikte önerilmiştir. Simülasyon sonuçları önerilen her iki yöntem için de yüksek sınırlandırma kazançları göstermiştir.

Anahtar sözcükler: Hava-yer, Doppler gecikme yayılım, DFT-S-OFDM.

Acknowledgement

I would like to thank all the people who shared in making this content available. Many thanks to Prof. Tuncer Baykaş, and my colleagues Morteza Soltani, Marwan Medhat and Murat Karabacak.

The work in Part 1 was supported by SAVRONIK under project number SV.SOZ.E/0043.14.008. The work in Part 2 was supported by ASELSAN under project number HBT-TE-2015-008.

Contents

List of Figures

List of Tables

Part I

Air-Ground Channel Model

Chapter 1

Air-Ground Doppler-Delay Spread Spectrum

1.1 Introduction

The demand for an Air-Ground (AG) wide band channel model is growing. Applications like ad-hoc networks with airborne mobile nodes for emergency situations or humanitarian missions, low flying air-base-stations, or unmanned military aircrafts will need highly reliable communication system design. Therefore, we need accurately characterized AG channel models. According to the comprehensive review [1] by D. Matolak, there is no accurate, validated model existing for Air-Ground channels. This motivates our study of AG communication link operation in the presence of both delay and Doppler spreads, presenting a Doppler-delay spread spectrum model for AG channels.

The Doppler-Delay-Spread Function was first presented by Bello [2] in the context of statistical characterization of wide sense stationary uncorrelated scattering (WSSUS) channels. In frequency selective time variant channels, the channel impulse response $h(\tau, t)$ is time dependent. Applying the Fourier transform to $h(\tau, t)$ with respect to time t, will give a Doppler-variant impulse response $p(\tau, f_d)$, called

the Doppler-delay spread spectrum, or scattering function as referred to in the literature [3]. A scattering function is sufficient to describe the dispersion caused by propagation delay τ and the Doppler shifts f_d jointly. Air-ground channels are categorized under non-WSSUS channels, therefore we can't use a stochastic model to model such channel. Instead of that, a geometric stochastic channel model (GSCM) approach is used in this study. Our aim in this model is to get a formula describing the Doppler-delay joint spectrum $p(\tau, f_d)$ as a function of positions of ground and air-station, and its three dimensional speed vector.

The following sections are organized as follows; some definitions are briefly presented in Section 1.2. Related work is discussed in Section 1.3. In section 1.4 the three dimensional geometric model along with the analytic derivations are presented, in section 1.5 a terrain based scattering function simulator is proposed, and in section 1.6 we show comparison between the results of the analytic model and the terrain based simulator. Finally the conclusions are Given in section 1.7.

1.2 Definitions

This section will go briefly through some of the important definitions essential for understanding the presented theory. For detailed explanation the reader is referred to the texts [4] and [3] .

1.2.1 Channel Impulse Response

In a multipath channel, the impulse response is a wideband channel characterization that contains all information necessary to simulate or analyze any radio transmission through the channel. This is due to the fact that the wireless channel can be modeled as a linear filter with a time varying impulse response $h(t, \tau)$. The time variation is due to the variation of the physical environment.

1.2.2 Power Delay Profile

For small scale channel modeling, the power delay profile $P_s(\tau)$ of the channel is found by taking the spatial average of $|h(t,\tau)|^2$ over a local area. By taking several measurements and averaging them, which removes the time variation and gives an accurate description of the scatterers effect on the transmission. The channel power delay profile is a useful characterization of the channel.

1.2.3 Doppler Spread Profile

Scattered signals arriving at the receiver will be Doppler shifted by different amounts depending on the angle that the arrival path makes with the direction of movement. Signals arriving from scatterers directly ahead of the receiver will be shifted higher in frequency; those directly behind will be shifted negatively by the same amount. The dependency on the angles of the scatterers and where they are positioned generates a unique Doppler power spread profile $P_s(f_d)$ that is environment dependent.

1.2.4 Scattering Function

Also called joint delay-Doppler power spread function $P_s(\tau, f_d)$, describes the relationship between delay shifts and Doppler shift for a specific environment. This stems from the fact that, in reality each scatterer has its own delay and Doppler shifts, and when summing the effect of all scatterers a joint relation appears, and its shape depends on the environment.

1.3 Related Work

This section presents the previous work in the literature that is related in theory or led to the development of this study. Looking at the Air-ground channel literature, Haas [5] and Elnoubi [6] discussed the 2-D delay-Doppler power spectrum $P_s(\tau, f_d)$, which is proportional to the joint probability density function $p(\tau, f_d)$ of Doppler spreading and delay spreading. It was assumed by Haas [5] that, the Doppler spread spectrum $p(f_d)$ is independent from the delay spread spectrum $p(\tau)$. As Shown in Figure 1.1, Haas assumed that in the landing phase the line of sight (LOS) path along with the scattered path components, mainly from buildings at the airport itself, can be modeled by a Rayleigh process. He also assumed that the Doppler spread spectrum results from scattered components that are not isotropically distributed but are assumed to arrive at the front of the aircraft. Which gives the shape shown in Figure 1.1.

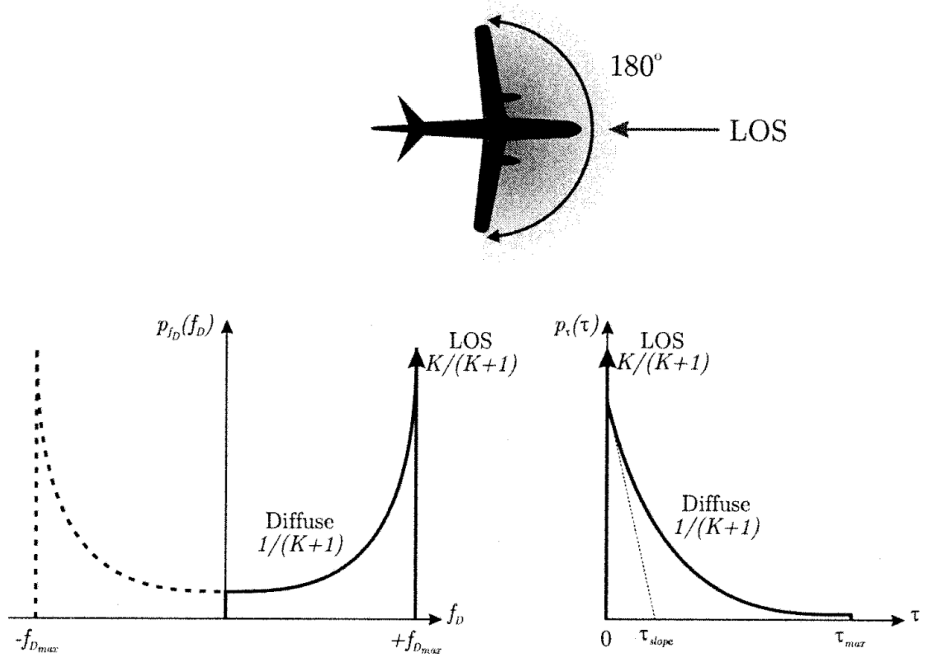

Figure 1.1: Haas's Doppler power spectrum and delay power spectrum for arrival scenarios.

However, we are inclined to disagree with Haas's assumptions because of measurement results in [7]. In this work measurements of scattering functions were taken during a the take-off phase of the flight. It was reported that the take-off and landing are the most sever channel phases. Figure 1.2 shows the scattering functions captured during this study. It can be seen that it begins with a moderate Doppler shift, then the Doppler spread gets worse as the velocity increases. After the take-off phase ends and the flight enters the en-route phase the scattering function returns to a Doppler shift again. This happens once the aircraft is far enough above the buildings.

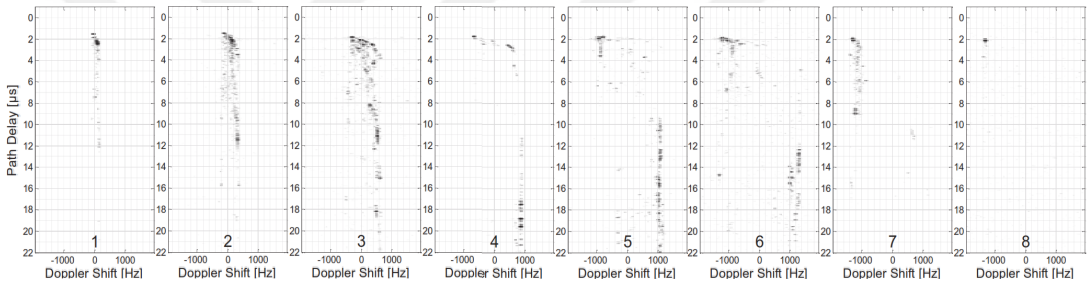

Figure 1.2: Eight subsequent snapshots of a take-off sequence

In [8] D. Cox presented a statistical description for Doppler-delay spectrum for multipath propagation in a suburban mobile radio environment. In [9] G. Acosta *et al.* presented a per-tap Doppler spectra for frequency selective vehicle to vehicle communication. In [10] S. Gligorevic *et al.* proposed a geometric based stochastic channel modeling approach to characterize the scattering function for airport environments. In [11] M. Walter *et al.* described Air-to-Air analytic Doppler-delay spectrum, as a function of the planes' positions, but it was limited only for 1-dimensional movements.

Then in [12] a GSCM delay Doppler density function for vehicle-to-vehicle communications was derived analytically, followed by [13] that presents a generalized Air-Air Doppler-delay spread model, which we will build our study on top of it after reformulating the distributions $p(l|\tau)$ and $p(\tau)$ because we don't agree with them. We will present a model for the air to ground dense scattering environments using a geometric model that was also used by [14] to derive a direction of arrival (DOA) and delay joint distribution. Our presented model is for low

altitude platforms, taking-off, landing or hovering over the ground station.

1.4 Model Geometry

In this section we present the geometric model, we assume that the air-station is moving at low altitudes above a dense scattering environment *e.g.*, urban areas. So, the model is for taking-off, holding, and landing air-craft phases. We are expecting diffused scattering from all over the area around the tower, assuming equal contribution from all that area, and equal vertical level for all scatterers. For the antennas we are assuming omnidirectionality at the tower and at the air-craft.

Line of sight (LOS) received signal component will be treated separately. The power ratio between LOS component and complete reflected components, is the well known Rice factor K_{Rice}, which is not well studied in AG links and needs to be characterized in future work. Values of K_{Rice} in VHF band where measured in [15] for AG links and they ranged between 2 dB to 20 dB.

The air-craft is separated from the tower by a ground distance $dist.$, and altitude hp, moving in 3-dimensions with 3 velocity components v_x, v_y, and v_z. The tower is h_t higher than the city level. From this basic geometry, we write an expression for the delay τ, as a function of the coordinates of the scatterers, and the air-craft position. We will do the same for the Doppler shift, then use the two expressions jointly to get a mathematical formula for the Doppler-delay spread spectrum.

The scattering point corresponding to the least delay, is taken to be the origin of the Cartesian coordinates, the plane and the tower lies on the same line at distances d and k away from the origin, as shown in Figure 1.3.

$$d = \frac{h_p * dist.}{h_p + h_t}, \quad k = \frac{h_t * dist.}{h_p + h_t}$$

The expressions for the system model will be written with this coordinate

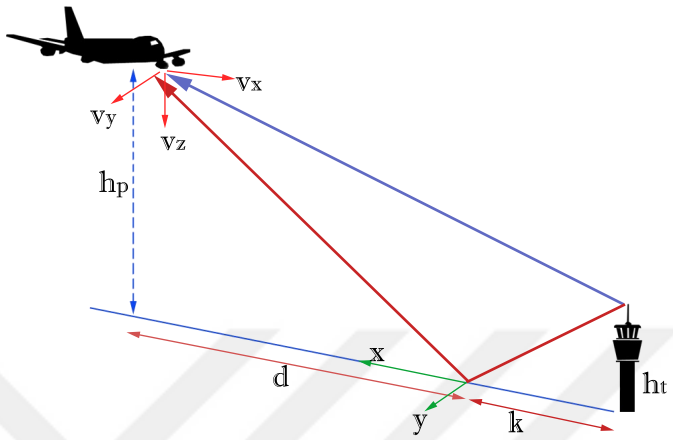

Figure 1.3: Geometric model

system. Taking the length of any scattered path $l = \tau.c$, the delay equations are

$$\tau_{LOS} = \frac{1}{c}\sqrt{dist^2 + (h_p - h_t)^2} \tag{1.1}$$

$$\tau(x,y) = \frac{1}{c}\left[\sqrt{h_t^2 + (k+x)^2 + y^2} + \sqrt{h_p^2 + (d-x)^2 + y^2}\right] \tag{1.2}$$

The Doppler shift of each path $f_d = v/\lambda$, where v is the rate of change in path length.

$$f_{d_{LOS}} = \frac{1}{\lambda}v_{LOS} = \frac{1}{\lambda}\frac{dl_{LOS}}{dt} = \frac{1}{\lambda}\frac{dist.v_x + (h_p - h_t)v_z}{\sqrt{dist^2 + (h_p - h_t)^2}} \tag{1.3}$$

$$f_d(x,y) = \frac{1}{\lambda}\frac{(d-x)v_x + y.v_y + h_p.v_z}{\sqrt{(d-x)^2 + y^2 + h_p^2}} \tag{1.4}$$

From (1.2) and (1.4), $p(f_d|\tau)$ and $p(\tau)$ will be derived, then multiplied together to get the joint probability density function $p(\tau, f_d) = p(f_d|\tau)p(\tau)$.

1.4.1 Delay Dependent Doppler Spread Spectrum $p(f_d|\tau)$

Our final goal in this section is to derive $p(f_d|\tau)$ from the space-dependent Doppler expression, and its distribution as will be shown. The delay expression draws elliptical contours on the x-y plane for different τ values. From (1.2) we can easily get the equation of this ellipse, function of delay:

$$y(x,\tau) = \pm\sqrt{ax^2 + bx + c} \tag{1.5}$$

where a, b and c are functions of τ, h_p, h_t, and $dist$. Substituting $y(x,\tau)$ in $f_d(x,y)$ expression we get the Doppler shift as a function of delay τ and x

$$f_d(x,\tau) = \frac{1}{\lambda}\frac{v_x(d-x) \pm v_y\sqrt{ax^2+bx+c} + h_p.v_z}{\sqrt{((d-x)^2 + ax^2 + bx + c + h_p^2)}} \tag{1.6}$$

According to [16], the distribution of f_d given delay $p(f_d|\tau)$, in terms of $p(x|\tau)$ is:

$$p(f_d|\tau) = \frac{p(x_1|\tau)}{f_d'(x_1|\tau)} + \frac{p(x_2|\tau)}{f_d'(x_2|\tau)} + \frac{p(x_3|\tau)}{f_d'(x_3|\tau)} + \frac{p(x_4|\tau)}{f_d'(x_4|\tau)} \tag{1.7}$$

where x_1, x_2, x_3 and x_4 are the roots of the inverse mapping of f_d to x. In our case, we will have 4 roots. We can get this inverse mapping and $f_d'(x,\tau)$ numerically, or we can derive a closed form from (1.4) . By substituting in (1.7) we will get the desired Doppler-given delay spread spectrum $p(f_d|\tau)$. Next, the distribution $p(x|\tau)$ will be discussed.

1.4.2 Deriving the Distribution of x, $p(x|\tau)$

We should derive $p(x|\tau)$ such that the probability of diffused scattering from any point on the ground is equal. According to [16] we can write the distribution of x as

$$p(x|\tau) = \frac{p(l|\tau)}{\left|\frac{dl}{dx}\right|} \tag{1.8}$$

solving this gives

$$p(x|\tau) = \sqrt{\frac{a(a+1)x^2 + b(a+1)x + (b/4+c)}{ax^2+bx+c}} \times \frac{p(l|\tau)}{norm} \tag{1.9}$$

where *norm* is a normalization factor, corresponding to the perimeter of the ellipse.

In [13], the probability of scattering from any point on the perimeter of the ellipse $p(l|\tau)$ is said to be uniform, but we disagree with this assumption. As shown in Figure 1.4 the contours of equal τ are plotted, the green cross represents the ground-station position, while the plane shape represents the air-station position. we can understand that the uniformity is violated specially for small ellipses, which correspond for early values of τ, because the ellipses are non-concentric. Hence, the contribution of scattering points falling on the circumference of the ellipse are not equal.

In this study an approximation is proposed for the distribution $p(l|\tau)$. We will assume that the distribution is linear as shown in Figure 1.4. The highest value of $p(l|\tau)$ is proportional to the changing rate of the ellipse's vertex x_{max}, with respect to the delay τ, $R_{xmax} = dx_{max}/d\tau$, and the lowest value proportional to $R_{xmin} = dx_{min}/d\tau$.

$$\begin{aligned} p(l|\tau) &= \begin{cases} \mathfrak{D}(x) & x \in [x_{xmin}, x_{xmax}] \\ 0 & otherwise \end{cases} \\ \mathfrak{D}(x) &= \frac{\frac{2(x-x_{min})(R_{xmax}-R_{xmin})}{x_{max}-x_{min}} + R_{xmin}}{R_{xmax}+R_{xmin}} \end{aligned} \tag{1.10}$$

The values of R_{xmax} and R_{xmin} can be calculated numerically from the equation of ellipse, or differentiated analytically from (1.5).

To compare the assumption of uniform $p(l|\tau)$ with our proposed distribution, we show a delay dependent Doppler profile in Figure 1.5, at a low delay. The

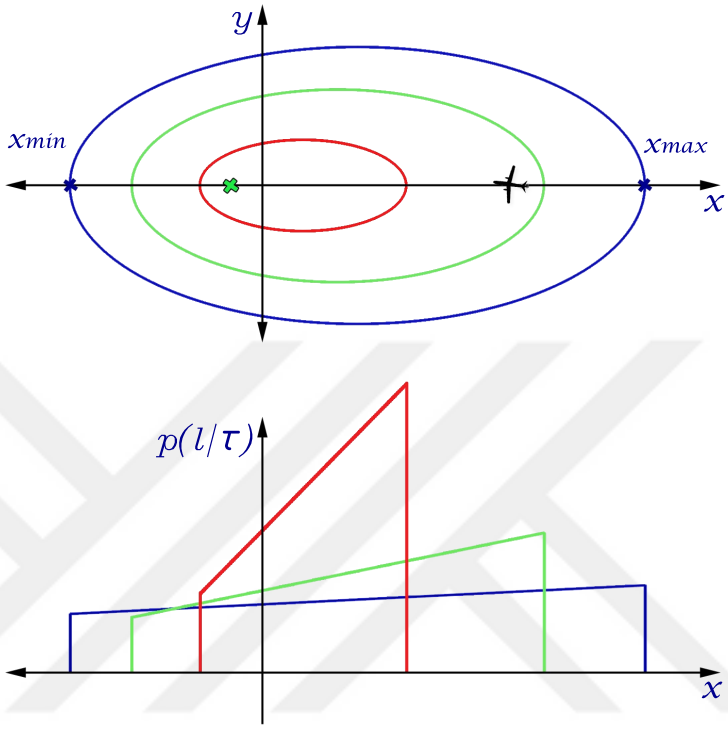

Figure 1.4: The proposed distribution of $p(l|\tau)$, for different delays.

blue colored distribution is calculated using the ray-tracing algorithm mentioned in Section 1.5, the red colored one is using the proposed distribution and the green colored one is plotted using the assumption of uniform $p(l|\tau)$.

1.4.3 Deriving the Marginal Delay Distribution $p(\tau)$

In this section we will derive the marginal distribution $p(\tau)$. It should be noticed that the propagation loss exponent is not involved in the mathematical derivation, and it should be multiplied by the derived $p(\tau)$ in case of channel emulation. The cumulative distribution of τ is simply the ratio of the area of the specified τ ellipse to the area of the τ_{max} ellipse.

$$CDF(\tau) = \frac{A|_{\tau}}{A|_{\tau max}}, \quad A = \frac{\pi}{\sqrt{-a}}[c - \frac{b^2}{4a}] \tag{1.11}$$

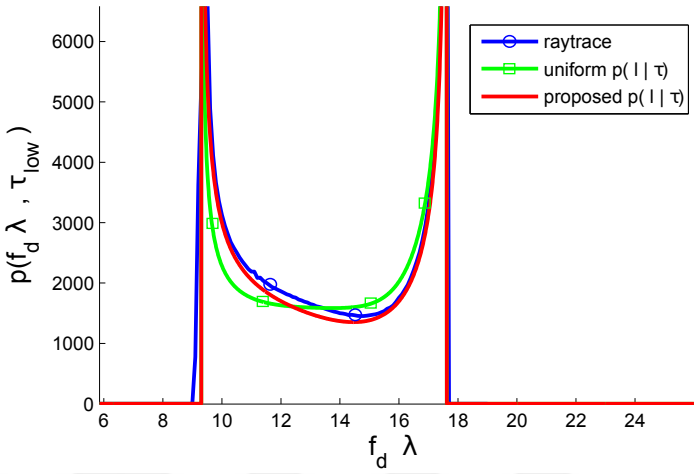

Figure 1.5: Comparing Doppler profiles for different $p(l|\tau)$ distributions

Notice that a is always a negative value and c is a positive value.

$$p(\tau) = \frac{dA|_\tau}{d\tau} \frac{1}{A|_{\tau max}} \tag{1.12}$$

$$\frac{dA}{d\tau} = \frac{dA}{da}\frac{da}{d\tau} + \frac{dA}{db}\frac{db}{d\tau} + \frac{dA}{dc}\frac{dc}{d\tau} \tag{1.13}$$

By direct substitution of τ and τ_{max} in (1.13), we get $p(\tau)$ which should be multiplied after that by the propagation loss exponent.

1.5 Terrain Based Doppler-Delay Model

The motivation for a terrain based model is that in real scenarios, mountains and valleys change the boundaries and shape of the scattering function. Also, the assumption that scattering rays from the ground contributes equally to the scattering function is violated, because mountains block some of the rays from reaching some regions on the ground. In addition to that, the scattering coefficients should depend on the type of the terrain that the diffused reflections are coming from, *i.e.*, an urban region, a rural region, and a sea surface, they all should have different scattering coefficients. Those scattering coefficients should

be characterized from real measurement campaigns. We leave this for a future study. One extra thing to add is the antenna patterns. A simulation based model will be flexible to modify its antenna patterns rather than being stuck with the omni-directional patterns, which give non-accurate estimate for the scattering function.

In this modified model, the regions shadowed by other higher regions will be removed from the scattering points set, then the scatterers elevations are added, which reformulate the delay and Doppler expressions as follows

$$\tau_{LOS} = \frac{1}{c}\sqrt{(h_a + z_a - h_g - z_g)^2 + (x_a - x_g)^2 + (y_a - y_g)^2} \tag{1.14}$$

$$f_{d_{LOS}} = \frac{1}{\lambda}\frac{(x_a - x_g).v_x + (y_a - y_g).v_y + (h_a - z_g).v_z}{\sqrt{(x_a - x_g)^2 + (y_a - y_g)^2 + (h_a - z_g)^2}} \tag{1.15}$$

where h_a is height of the plane relative to z_a and h_g is the height of the ground tower relative to z_g. The values z_a and z_g are the altitudes of the terrain points corresponding to the air-craft and the ground tower positions, respectively. The coordinates (x_a, y_a) and (x_g, y_g) are the positions of the air-craft and the ground tower respectively.

Then the $\tau(x, y)$ of the scattered rays as a function of the position of the scatterer will be

$$\begin{aligned}\tau(x, y) \quad = \quad & \frac{1}{c}(\sqrt{(h_a + z_a - z)^2 + (x_a - x)^2 + (y_a - y)^2} \\ & + \sqrt{(h_g + z_g - z)^2 + (x_g - x)^2 + (y_g - y)^2}\ )\end{aligned} \tag{1.16}$$

and $f_d(x, y)$ of the scattered rays as a function of the position of the scatterer will be

$$f_d(x, y) = \frac{1}{\lambda}\frac{(x_a - x).v_x + (y_a - y).v_y + (h_a - z).v_z}{\sqrt{(x_a - x)^2 + (y_a - y)^2 + (h_a - z)^2}} \tag{1.17}$$

A basic single-bounce ray tracing algorithm is used to remove those sight blocked regions from the scatterer points set. We set the tower as the center of spherical coordinates, then scan the terrain as shown in algorithm 1, and remove the points that doesn't satisfy the condition presented. The terrain elevation values $z(\phi, r)$ can be extracted from digital elevation model (DEM). The red dashed region in Figure 1.6 represents the removed points.

Algorithm 1 Removing shadowed regions

procedure SCAN TERRAIN
  $\theta = -90^o$ ▷ initially
  for $\phi = 0$ to 360^o **do**
    for $r = 0$ to edge of map **do**
      if $(z(\phi, r) - h_{twr}) \geq r tan(\theta)$ **then**
        $\theta = \arctan(\frac{z(\phi, r) - h_{twr}}{r})$ ▷ update θ
      elseremove the point (ϕ, r) from the set
      end if
    end for
  end for
end procedure

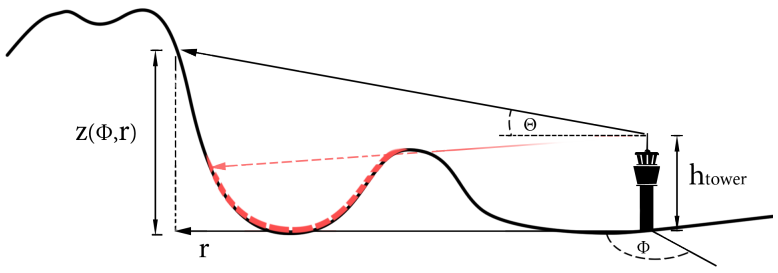

Figure 1.6: Geometry of shadowed-regions-removal algorithm

We apply the values of the terrain altitudes into (1.16) and (1.17) for the scattering points set, and that gives us another set of τ and f_d values. We use these sets jointly, to get a numerical joint frequency function, and that will be the required terrain based scattering function.

1.6 Results

In this section we will show the results of the terrain-based Doppler-delay spread model and the analytic air-ground Doppler-delay spread model side by side. For both models, the air-station will be at altitude 700 m, and 1500 m away from the ground-station. The ground station height is 50 m. The air platform speed components are $v_x = 15\ m/s$, $v_y = 10\ m/s$, and $v_z = 5\ m/s$ which are relatively low speeds for air crafts, but fair for aerial base stations.

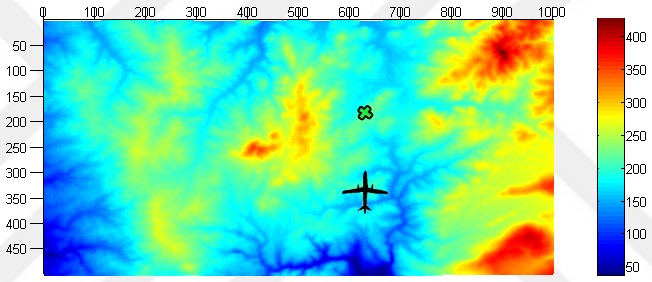

Figure 1.7: DEM of Kocaeli, Turkey, scale 1:20

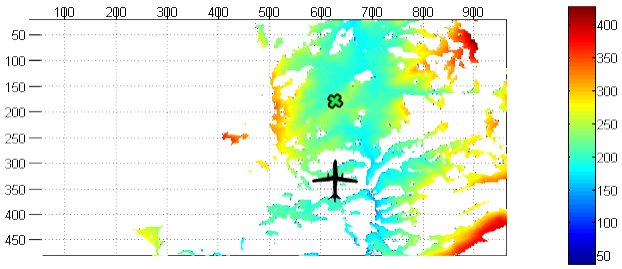

Figure 1.8: Result of shadowed areas removal algorithm

For the terrain simulations we use DEM for a hilly terrain area in Kocaeli, Turkey. As shown in Figure 1.7. The ground-station is 216 m above sea-level, and we have 400 m above sea-level mountains, and 150 m above sea-level valley. The position of the ground station is shown on the figure as a green cross, with the air platform shown below it. The result of the shadowed regions removal algorithm is shown in Figure 1.8.

The comparison between the Doppler-delay spread spectra of the analytic

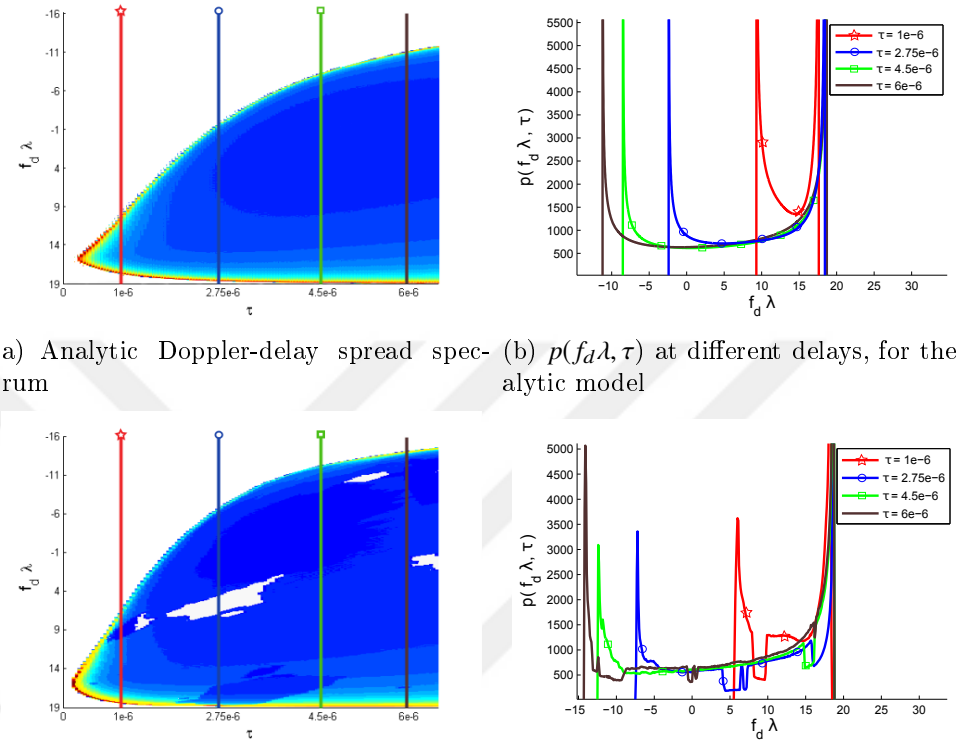

(a) Analytic Doppler-delay spread spectrum

(b) $p(f_d\lambda, \tau)$ at different delays, for the analytic model

(c) Terrain-Based Doppler-delay spread spectrum

(d) $p(f_d\lambda, \tau)$ at different delays, for the terrain based model

Figure 1.9: Analytic vs terrain-based Doppler-delay spread spectrum results

model, and the terrain based model is shown in Figure 1.9 normalized with respect to carrier frequency. We observe that the scattering function is unique for each terrain and position of ground station and air station. It's also observed that mountains-even if not high- can make the Doppler-delay spread spectrum wider. Because, high altitude scatterers will contribute higher Doppler shifts than its delay equivalents at lower altitudes. Regions that are blocked don't contribute to the scattering function, and will result in a non-continuous Doppler profile.

1.7 Conclusion

In this study we presented a three dimensional geometric stochastic channel model (GSCM) for Air-Ground Doppler delay spread spectrum. Reformulated the conditional distributions of scatterers on delay-contour segments, and the marginal delay distribution, found in the literature. Also we proposed a numerical terrain based Doppler-delay spread model simulator. Finally, we compared the analytic model, with the terrain based Doppler-delay simulator results. We found that the terrain topography affects the shape of the Doppler-delay spread spectrum, and it becomes unique for each terrain and position of ground station and air station.

Part II

Well Contained Signals

Waveforms are the physical shape of the analog signal that carries information. The shape of the waveform gets generated from the data and the pulse shapes involved in forming the waveform. Waveforms are evaluated based on some key performance parameters, like spectral efficiency, and peak to average power ratio (PAPR). Waveform Containment or localization are one of the critical performance parameters, as it shows how much a signal is leaking or interfering with neighboring signals. Depending on the system requirements, signal containment sets the need for guards in frequency or time domains; hence it is correlated with the spectral efficiency parameter. A well-localized symbol can be formed from well-contained pulses. In the literature, there are many proposed pulse shapes [17] each with its spectral efficiency vs. containment compromise. Pulses with the lowest side lobes have the least spectral efficiency. The containment of a waveform is evaluated over the whole symbol, with all the pulses combined. Mixing different pulses in the same symbol would be a good idea because it will allow using high contained low spectral efficiency pulses only at the edges of the signal band. However, it does not ensure orthogonality between the pulses, because each pulse occupies the time-frequency space uniquely.

This part is dedicated to new techniques for signal containment. The main Idea is mixing different pulse shapes with different parameters in the same signal. In Chapter 2, a modulation scheme that mixes raised cosine pulses with different roll-off factors α is proposed. The scheme is called Zero Tail Filter Bank Spread OFDM (ZT FB-S-OFDM) because it uses filter banks to generate raised cosine shaped pulses with α values of 1 and 0 in the same signal. The abrupt transition between the roll-off factors maintains orthogonality between pulses and puts the pulses with high α values on the edges of the signal. However, the pulses with $\alpha = 1$ have half the spectral efficiency of the pulses with $\alpha = 0$. This means that it is expected to have a compromise between spectral efficiency and signal containment, but the results show enhanced performance comparing the proposed scheme with the conventional schemes at the same spectral efficiency. In Chapter 3, the technique is taken one step further. Instead of the abrupt transition between the roll-off factor values, a smooth transition is proposed. The orthogonality is maintained by introducing the principle of time-frequency space

wrapping. The smooth transition between the roll-off factors allows for more enhanced performance than the one gained in the case of the abrupt transition in ZT FB-S-OFDM.

Chapter 2

Zero Tail Filter Bank Spread OFDM

2.1 Introduction

The vision for 5G systems includes a large variety of applications with demanding performance requirements. Besides the desire for more data rates, there will be a demand for services with high mobility. This requires systems with higher Doppler spread immunity. Tactile Internet will require ultra low latency systems. Internet of Things (IoT) will require ease of synchronicity, hence lower out-of-band emission (OOBE) is required, as well as power and cost-efficient implementations. The support of multi-input and multi-output (MIMO) systems, beam-forming and mm-wave technologies is also important. These requirements push the limits of the current orthogonal frequency division multiplexing (OFDM) systems beyond its capabilities. Several useful improvements over the conventional OFDM system have been proposed in the literature. A Scheme like filtered-OFDM [18] aims at easing synchronicity requirements, while keeping the inter-symbol interference (ISI) and inter-carrier interference (ICI) within acceptable limits. Generalized Frequency Division Multiplexing (GFDM) [19] features low PAPR compared to OFDM, and lower OOBE. Universal Filtered

Multi-Carrier (UFMC) [20] aims at easing synchronicity requirements too. Filter Bank based Multi Carrier (FBMC) [21] applies filtering per subcarrier to achieve signal containment in time and frequency domains. All of the aforementioned waveforms have their own advantages and disadvantages, and the comparison of them is out of the scope of this work.

In this study, a single carrier (SC) system is presented and motivated based on its simplicity and efficiency. In terms of power, SC systems exhibit lower PAPR values, and for channel impairments, they are less sensitive to carrier frequency offsets. The proposed system is called Zero Tail Filter Bank Spread OFDM (ZT FB-S-OFDM). It is an improved version of Zero Tail Discrete Fourier Transform Spread OFDM (ZT DFT-S-OFDM). An additional flexibility is proposed over the spreading technique, solving the problem of non-perfect zero-tails in ZT DFT-S-OFDM. In the classical DFT-S-OFDM [22], the time symbol has a cyclic prefix (CP) to convert the linear convolution of the channel into a circular convolution, for simplifying frequency domain channel estimation and equalization. In ZT DFT-S-OFDM the cyclic prefix is replaced by a zero-tail. Unlike cyclic prefix, it is flexible in length and can be adjusted to match the channel time spread requirements. Moreover, by using zero-tails instead of CP, the waste of power over CP part is saved.

Unique word (UW-) OFDM [23] replaces CP with a unique word that can be set to be a zero-tail. The advantage of ZT DFT-S-OFDM over UW-OFDM is the lower computational complexity to introduce a zero-tail. As ZT DFT-S-OFDM is a single carrier scheme, adding a zero-tail is as simple as adding zeros as symbols. In addition, UW-OFDM has a power penalty of the redundant sub-carriers.

In ZT DFT-S-OFDM, the time domain pulses leak into the zero-tail portion of the symbol. This non-perfect zero-tail leaks power to the consecutive ZT DFT-S-OFDM symbol, in presence of time-dispersive channels. This makes the performance ISI limited rather than being noise limited. Therefore, the main motivation in the proposed scheme is to suppress the leakage of zero-tail to the consecutive ZT DFT-S-OFDM symbol. In ZT FB-S-OFDM, the DFT block is

replaced by a filter bank multicarrier block. This enables the shaping of each pulse on its own, hence having different pulse shapes in the same stream. Two pulse shapes will be mixed in this system, sinc-shaped pulses and raised cosine (RC) shaped pulses. RC-shaped pulse is chosen for its low side lobes and capability of being orthogonal with sinc-shaped pulses.

The chapter is arranged as follows: Section 2.2 discusses the conventional ZT DFT-S-OFDM. The proposed ZT FB-S-OFDM scheme is presented in Section 2.3. In section 2.4, a simple implementation technique for the transmitter and the receiver is presented. Section 2.5 is reserved for simulations and results and Section 2.6 for the conclusion.

2.2 ZT DFTs-OFDM System

A Zero Tail DFT-Spread OFDM [24] system structure is similar to the traditional DFT-S-OFDM [22] system. They share the same transmitter and receiver structures, and same performance characteristics, such as low PAPR and frequency domain channel equalization (FDE) capability. DFT-S-OFDM is a single carrier scheme where data symbols go through a DFT block of order M followed by an IFFT of order N. This process is equivalent to taking the complex data symbols from the time domain to frequency domain then back to the time domain after spreading them with a factor of N/M. In other words, DFT-S-OFDM spreads each complex symbol into an up-sampled pulse shape. Due to the inherent rectangular shape of DFT and IFFT windows, the resulting pulses are sinc-shaped in the time domain.

In order to apply frequency domain equalization, the cyclic nature of the signal should be preserved. This is one of the reasons that CP extension has been considered for OFDM and DFT-S-OFDM systems. On the other hand, ZT DFT-S-OFDM replaces this cyclic prefix with a zero-tail. The zero-tail is introduced as a part of the modulated symbols. The system spreads the complex data symbols to sinc-shaped pulses which power decays slowly with time. As a result, the power

over data pulses leaks into the zero-tail portion, which causes the existence of non-perfect zero-tails.

Figure 2.1: Zero-tail of the first symbol is interfering with the second symbol

Non-perfect zero-tails cause power leakage into the consecutive ZT DFT-S-OFDM symbol, in the presence of time dispersive channels, as shown in Figure 2.1. Therefore, the system performance becomes ISI limited rather than being noise limited. In other words, an error floor due to the ISI is observed in the bit error rate (BER) performance. In the conventional system, to avoid power regrowth at the tail zero-heads are added. To decrease the power leaked from zero-tails further, the zero-heads length can be extended. In the next section, the proposed scheme will be introduced as a solution to reduce the power over the zero-tails.

2.3 Zero Tail Filter Bank Spread OFDM

Using filter banks for multicarrier modulation was first introduced in the literature even before the invention of OFDM [25]. In the proposed scheme shown in Figure 2.2, the DFT block in the conventional DFT-S-OFDM is replaced with a filter bank block. A bank of subcarriers enables the system to shape each pulse on its own in time domain. Allowing the use of pulses that is more contained in the time domain. Thus, data symbols contribute less power leakage to the zero-tail region.

Other Nyquist pulses can be introduced to replace the sinc-shaped pulses. The proposed is to let sinc-shaped pulses coexist with other raised cosine-shaped pulses of other α values, all in the same stream, without breaking the orthogonality condition.

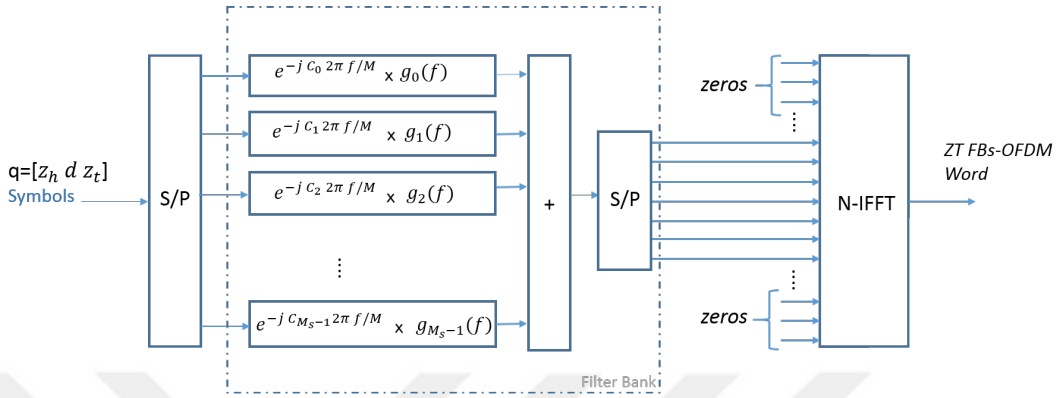

Figure 2.2: Transmission system of Filter Bank Spread OFDM

To describe this system in equations, the input complex symbols vector q is

$$q = [z_h \; data \; z_t] \tag{2.1}$$

where z_h and z_t are the zero-heads and zero-tails respectively. The output of the filter bank will be

$$FB(f) = \sum_{m=0}^{M_s-1} q(m)\; e^{-jC_m 2\pi f/M} g_m(f) \tag{2.2}$$

where M_s is the number of the input symbols, C_m decides the subcarrier increments in the frequency domain, and accordingly the place of the pulse in time domain, $g_m(f)$ is the shape of the filter (or the window in frequency domain). Like DFT, f is defined as $f = 0, 1, \cdots, M-1$. So, $g_m(f)$ is also a vector with M samples, and the filter bank block is represented by an $M_s \times M$ matrix. Finally, the output of the filter bank is applied to the IFFT block and the output word is as follows:

$$word(t) = IFFT(FB_{M_s \times M} \times P_{M \times N}) \tag{2.3}$$

where $P_{M \times N}$ is the mapping matrix that represents the mapping operation before the N-sized IFFT block, and as before $N > M$.

In the time domain, an RC-shaped pulse with high α value is more contained than one with low α. This means that using a high valued α pulses near the zero-tails is preferred, as it leaks less power to the tails. On the other hand, the

inner pulses are not critical. But, using higher α causes the pulses near the edges to take more bandwidth than the assigned resource block bandwidth. To Keep all the pulses within the same bandwidth, RC-shaped pulses need to be extended in time with the same α factor.

In the proposed waveform, the pulses that are located around the edges, are assumed to be RC shaped with a roll-off factor of 1. In order to make these pulses orthogonal to the sinc-shaped pulses and at the same time preserving the same bandwidth, in the time domain, they are extended to have twice the period of the inner pulses, as shown in Figure 2.3. The mathematical proof for orthogonality is given in the Appendix. The data symbols shaped with RC pulses are referred to as r_h for the heads region, and r_t for the tails region. The data symbols shaped with the sinc filter are referred to as s.

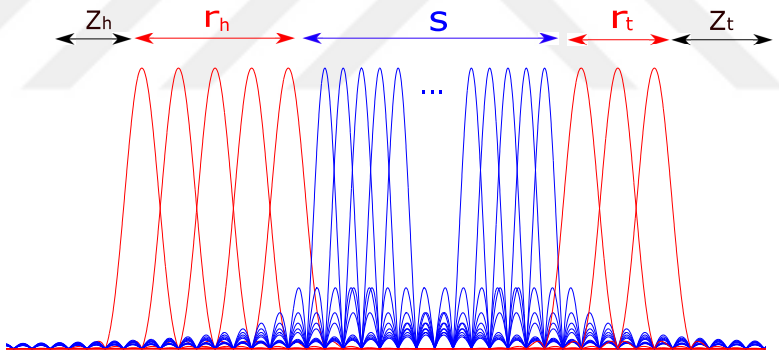

Figure 2.3: Pulse structure at the transmitter

In the conventional system, the parameters in (2.2) are as follows: C_m are increments of integer numbers and $g_m(f)$ are square-shaped windows. However, in the proposed scheme, they change over m values as follows:

$$c_m = \begin{cases} m & ; m < z_h \\ 2m - z_h & ; z_h \leqslant m < z_h + r_h \\ m + r_h & ; z_h + r_h \leqslant m < z_h + r_h + s \\ 2m - s - z_h + 1 & ; z_h + r_h + s \leqslant m < M_s - z_t \\ m + r_h + r_t & ; M - z_t \leqslant m < M_s \end{cases} \tag{2.4}$$

$$g_m(f) = \begin{cases} RC\ window & ; m < z_h + r_h \\ 1 & ; z_h + r_h \leqslant m < z_h + r_h + s \\ RC\ window & ; z_h + r_h + s \leqslant m < M_s \end{cases} \tag{2.5}$$

where M_s the total number of modulated symbols

$$M_s = z_h + r_h + s + r_t + z_t. \tag{2.6}$$

It is obvious that the number of transmitted data symbols decreases by $(r_h + r_t)$ to enhance the BER performance. Alternatively, this can be done in the conventional system by increasing the value z_h and z_t lengths [24]. Therefore, the simulation section needs to show that the proposed scheme outperforms the conventional scheme for the same number of data symbols.

2.4 Implementation and Complexity

The complexity of implementation is one of the distinguishing factors among different schemes. When choosing a scheme, there is always this compromise between performance and computational complexity. Filter banks are computationally consumptive and add complexity to the implementation. Filter banks were implemented with polyphase networks in [26]. However, the roll-off factor values are proposed to alternate between 0 and 1, as discussed in the previous section. This α profile makes it easy to implement the scheme with FFT blocks rather than polyphase structures as shown Figure 2.4.

We shall split our data symbols among two superimposing groups D_1 and D_2. The one that we intend to shape as raised cosine pulses are passed through a DFT followed by an RC windowing function. The rest of the data symbols are passed through another DFT block. Both DFT blocks have the same M-size and identical subcarrier spacing. Similar to the conventional system $N > M$. Input

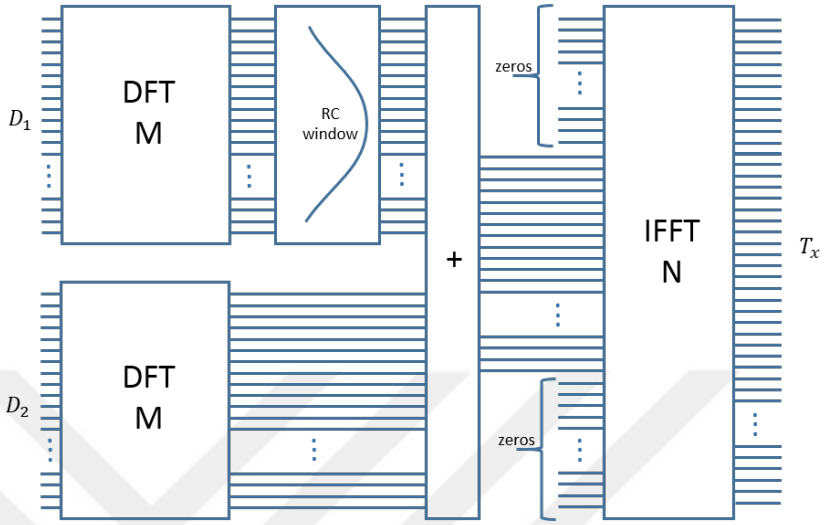

Figure 2.4: Transmitter implementation

vectors are

$$D_1 = [zeros(z_h)\ \ d_0\ \ 0\ \ d_1\ \ 0\ \ d_2\ \ 0 \ldots d_{r_h-1}\ \ 0\ \ \ zero(s)\ \ \ 0\ \ d_{s+r_h}\ \ 0\ \ d_{s+r_h+1} \ldots \\ 0\ \ d_{s+r_h+r_t-1}\ \ \ zeros(z_t)]^T \tag{2.7}$$

$$D_2 = [zeros(z_h + r_h)\ \ d_{r_h}\ \ \ d_{r_h+1}\ \ \ d_{r_h+2} \ldots d_{r_h+s-1}\ zeros(r_t + z_t)]^T. \tag{2.8}$$

From (2.7) and (2.8), the data symbols belonging to the r_h and r_t regions are separated by zeros between each two symbols. This is due to the fact that each corresponding pulse occupies twice the time than the sinc-shaped pulses do. The size of the DFT blocks M will be

$$M = z_h + 2r_h + s + 2r_t + z_t. \tag{2.9}$$

The receiver architecture is the inverse of the transmitter. In addition to that, a frequency domain equalization block exists right after the FFT block as shown in Figure 2.5. Note that the received R_h and R_t regions are now oversampled, and each two useful data symbols are separated by a value $\times$ that shall be discarded. Data symbols will be picked from the same positions that are placed beforehand on the transmitter side.

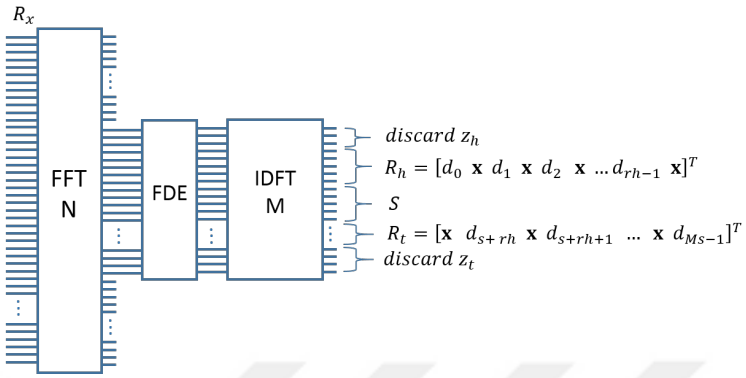

Figure 2.5: Receiver implementation

2.5 Simulations and Results

In order to get more understanding of how does ZT FB-S-OFDM scheme perform compared to the conventional scheme, this section will simulate 4 main aspects. First one is the leakage caused by non-perfect zero-tails for different z_h, z_t, r_h and r_t values. Second, BER performance of the proposed scheme is given. Third, the PAPR performance and the effects on the PA efficiency is discussed. Finally, the spectral containment is described. It was explained that by increasing r_h and r_t, the length of data symbols is reduced. For a fair comparison, results compare the proposed and the conventional system with the same data symbol rate.

2.5.1 Non-Perfect Zero-Tail Leakage Contours

In the conventional scheme, there is the option to extend z_h and z_t to decrease the power over the zero-tails. The following contours compare this with the option of extending r_h and r_t, in the presence of time-dispersive channels. An exponential power delay profile and a uniform power delay profile are used for this section. Simulation parameters are $M = 144, N = 512$ and channel is a multipath Rayleigh fading channel, with exponentially decaying and uniform power delay profiles (PDP); for the uniform channel $\tau_{max} = 40T_s$, and for the exponential channel $\tau_{rms} = 11.5T_s$. These values are referred to sample duration T_s.

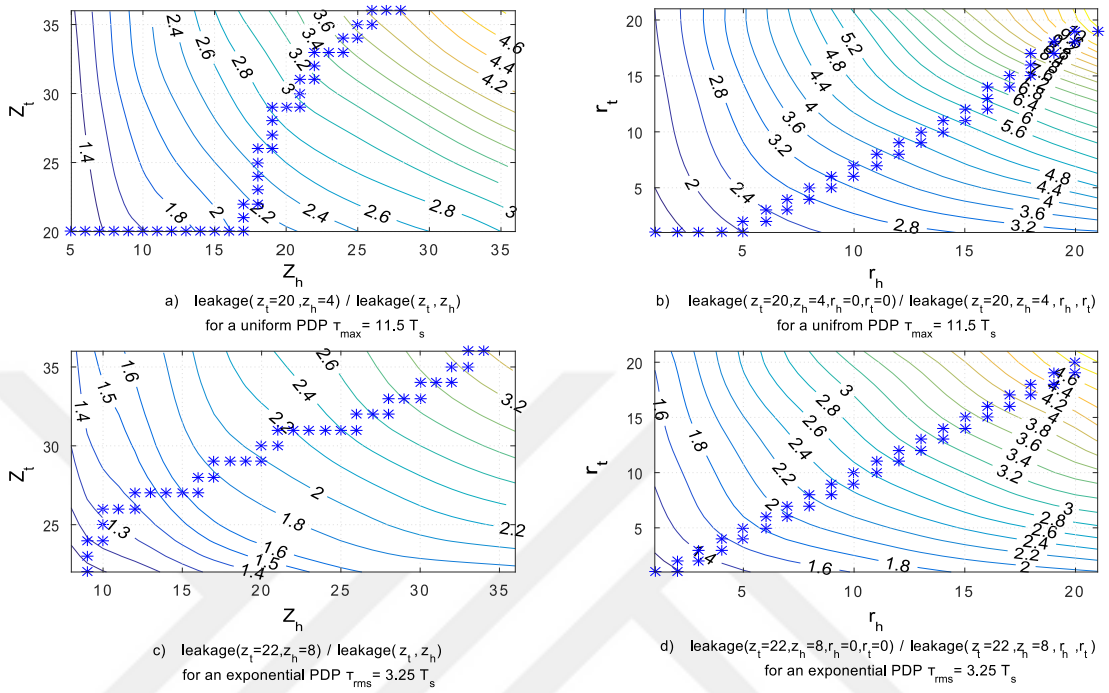

Figure 2.6: Contours describing the gains in leakage reduction for extending z_h, z_t in the conventional system, and r_h, r_t in the proposed system

In this section, the function *leakage*() is defined, which calculates how much power is leaked from the non-perfect zero-tails to the consecutive ZT FB-S-OFDM symbol, due to channel dispersion. Figure 2.6 shows leakage gains for different z_h, z_t, r_h and r_t values compared to the leakage of higher leakage operation points. To clarify, Figure 2.6(a) shows the contour of the gain function: $gain = leakage(z_t = 20, z_h = 4)/leakage(z_t, z_h)$. It is shown that all the points with $z_t > 20$ and $z_h > 4$ have less leakage than the reference point $leakage(z_t = 20, z_h = 4)$. They also have less throughput due to the loss of data symbols either because of extending $(z_h + z_t)$ or $(r_h + r_t)$. Hence, there is a compromise between less leakage and more throughput. The contours show a trajectory of points of operation (z_h, z_t) for the conventional system, and (r_h, r_t) for the proposed system. Marked by stars in Figure 2.6, these trajectories of points satisfy the least leakage for a specific throughput.

Next, the gain of extending r_h and r_t over extending z_h and z_t is shown in Figure 2.7. We define the variable l as the extension of (z_h+z_t) in the conventional system

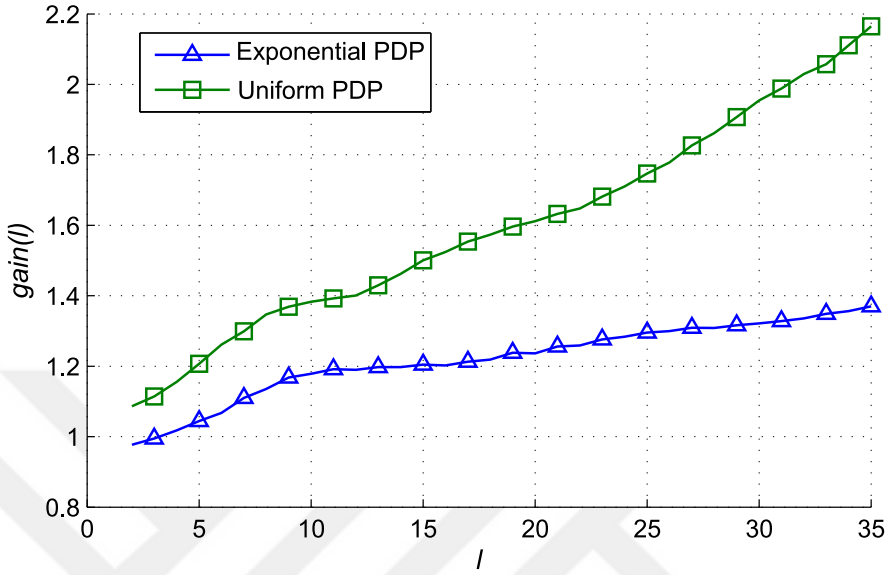

Figure 2.7: Gain in leakage reduction, of the proposed system, vs degradation in throughput "l".

or the extension of $(r_h + r_t)$ in the proposed system. The points with the same throughput (marked with stars in Figure 2.6) are picked to show the gain over the conventional system.

2.5.2 BER Performance Evaluation

In this part, the system is evaluated in a multipath Rayleigh fading channel, with exponentially decaying PDP. The rms delay spread is $\tau_{rms} = 7T_s$. Results for a uniform PDP with maximum excess delay of $\tau_{max} = 40T_s$, is also presented. Where T_s is the sample duration. The interference is simulated with two consecutive QPSK modulated ZT FB-S-OFDM symbols. The zero-tail of the first ZT FB-S-OFDM symbol leaks into the second symbol and degrades its performance.The simulations are based on evaluating the performance of the second ZT FB-S-OFDM symbol. Both symbols have the same z_t, z_h, r_h and r_t. Full channel knowledge at the receiver is assumed. Zero-forcing FDE equalization is performed. From the previous section, the points of operation are shown in the legend of Figure 2.8. It is obvious that the conventional system suffers from

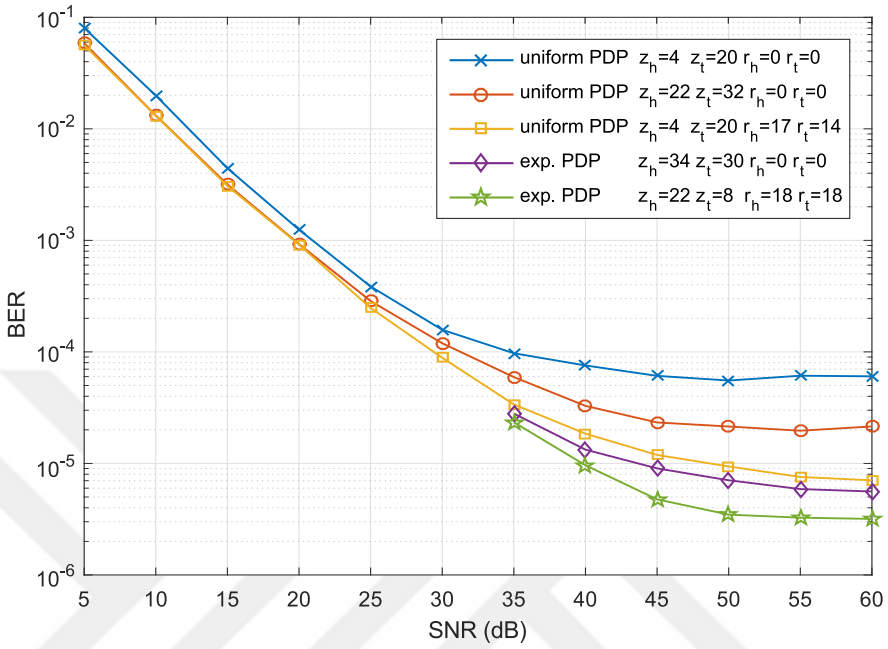

Figure 2.8: BER vs SNR with different channel PDPs, M=144 N=512.

higher error floor in BER performance, which means that the system performance is ISI limited. Therefore, the less the leakage, the less the interference and the better the BER performance. We can see that the system exhibits higher gains in a uniform delay spread profile channel.

2.5.3 Power Amplifiers and PAPR

For the zero-tail category of signals, it is useful to treat the signal as a multimode signal, each mode with its own PDF and PAPR values. Power amplifiers can operate at different backoff values for each mode. Among the several techniques of PA design, Envelope tracking is the best for multimode operation [27]. In this line of thought, the complementary cumulative distribution function (CCDF) of the PAPR is calculated, for the sinc-shaped pulses region separately from the RC-shaped pulses region. This also means that the length of the zero-tail region does not affect the CCDF because it is considered as a separate mode of operation. Figure 2.9 shows that the RC-shaped pulses region have better PAPR than the sinc-shaped pulses region, and the PA can operate with higher efficiency

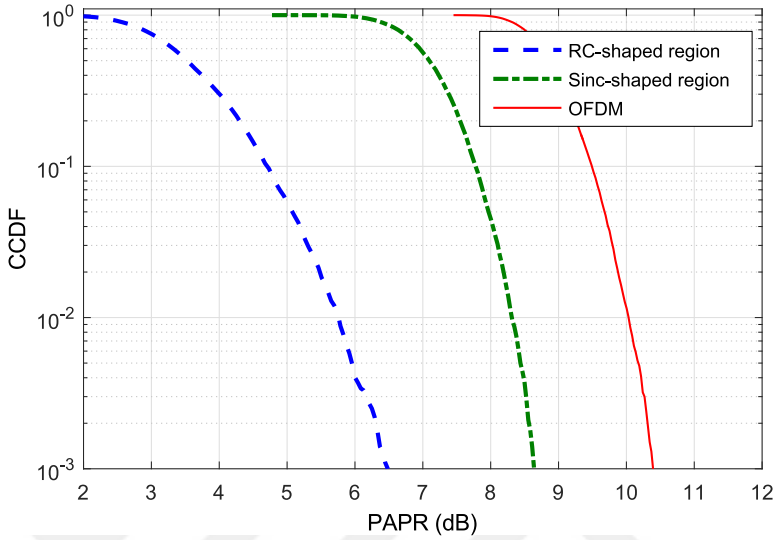

Figure 2.9: CCDF of PAPR for the two regions of operation

in the RC-shaped pulses region. So, an improvement in terms of PA efficiency is achieved, depending on the ratio of $r_h + r_t$ to the time duration of the signal.

2.5.4 Spectral Containment

In OFDM and DFT-S-OFDM systems, abrupt transitions between symbols in the time domain causes high OOBE in the frequency domain. In the case of ZT DFT-S-OFDM technique, the transitions are from the zero-tails of one ZT DFT-S-OFDM symbol to the zero-heads of the consecutive symbol. Thus, the usage of zero-tails and zero-heads decreases the effect of abrupt transitions between symbols. In ZT FB-S-OFDM, due to decreasing the power of zero-tails and zero-heads, the abrupt transitions are lower. As a result, the OOBE is lower than the conventional ZT DFT-S-OFDM, as shown in Figure 2.10. This is an advantage over the systems that uses CP because low OOBE became an inherent property in the signal without the need of additional windowing.

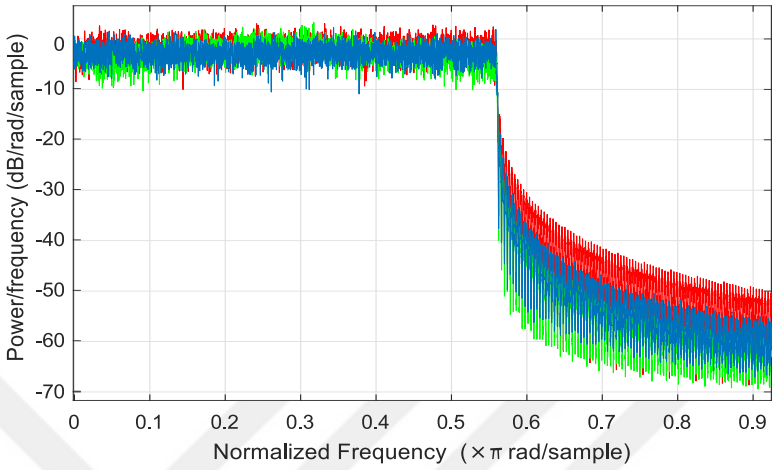

Figure 2.10: Power spectral density estimates for both systems.

2.6 Conclusion

A new scheme called Zero Tail Filter Bank spread OFDM is proposed. The scheme enables mixing different pulse shapes in the same stream. In this study, it is specifically proposed to have raised cosine-shaped pulses with sinc-shaped pulses side by side in the same symbol. This introduces an enhancement over the conventional ZT DFT-S-OFDM. Replacing sinc-shaped pulses with RC-shaped pulses near zero-tails reduces tails leakage significantly and keeps the orthogonality between both pulses. Also, an implementation technique using FFT and IFFT blocks was presented. Then, in the simulation section, the lengths of RC regions r_h and r_t with the tails z_h and z_t are shown to have optimum values. Contours of these values are shown with different channel power delay profiles. In conclusion, reducing the zero-tail leakage improves the BER and OOBE performance. Furthermore, we learn that the RC-shaped region of the proposed waveform offers better PAPR, hence, higher power efficiency.

Chapter 3

Time-Frequency Space Warping For Well-Localized Signals

3.1 Introduction

In Orthogonal Frequency Division Multiplexing (OFDM) systems [28] the rectangular shaped window of the time domain symbol, results in sinc-shaped subcarriers. Side-lobes power of a sinc shapes subcarrier dies slowly. Therefore, the subcarriers on the edges of the spectral band leak significant power out of the assigned band. This leakage is referred to as Out-Of-Band Emission (OOBE). In single carrier systems, like Zero-Tail Discrete Fourier Spread OFDM (ZT DFT-S-OFDM) [24] the mapping to the IFFT is a rectangular shaped window. So, pulses in the time domain are sinc-shaped. Meanwhile, a portion of the ZT DFT-s-OFDM symbol is zeroed out as a guard period, instead of a cyclic prefix. Again, the side lobes of sinc-shaped data pulses leak into the zero-tail portion, causing performance degradation in the presence of a time dispersive channel. Suppressing zero-tail in the case of single carrier systems, or OOBE in multi-carrier systems is vital for interference suppression and better performance in communication systems.

In the literature, there are many techniques to get lower power sidelobes in time or frequency domains. The simplest of them is to assign null pulses or guard subcarriers at the edges of the data stream or the spectral band [29]. Time domain windowing is also a widely used solution [30],[31], it transforms the sinc-shaped pulses into pulses with faster-decaying side lobes. However to keep the orthogonality the symbol duration needs to be extended, hence the loss in spectral efficiency. Non-orthogonal windowing was also proposed in the literature as in filtered-OFDM scheme [18]. However, windowing the entire symbol is a waste of resources, because pulses are treated equally while they don't contribute equally to sideband emissions. In the direction of using different pulses in the same stream, it was proposed in [32] to have raised cosine (RC) shaped subcarriers with different roll-off factors α along the subcarriers, but orthogonality was sacrificed. In the work presented in Chapter 2 [33], orthogonality was kept, by using two sets of raised cosine shaped pulses in the same stream, with the higher contained pulses ($\alpha = 1$) on the edges, and the less contained ($\alpha = 0$) in-between, because pulses on the edge contribute more to the sidelobes. Therefore, it is useful to use the roll-off factors of RC pulses as a degree of freedom to suppress the sidelobes of the waveform, allowing a smooth transition of roll-off factors along the pulses. But if the pulses need to have the same occupancy in the transform domain, it will harm the orthogonality. The only way not to miss with the orthogonality is to introduce an extra degree of freedom to compensate for the roll-off-factors change along the pulses.

Axis warping principle [34] is proposed as an additional degree of freedom to contain the signal. The idea is to use pulse shapes with low side lobes at the edge of the signal band, which occupy more space in the transform domain. Time-frequency space warping can be used to shrink the transform domain at the edges, to compensate for the extension introduced by roll-off factors, without affecting the orthogonality. With this technique, a smooth roll-off factor profile can be used, which was not possible previously without affecting the orthogonality. This work also falls under the context of nonuniform sampling [35] and nonuniform filtering.

Next section, the axis warping principle is explained, showing its effect on the

time-frequency lattice. Then in Section 3.3, implementation of time-axis warping for single carrier (SC) systems is proposed. Followed by generating the warping function in Section 3.4. Which is based on an optimum roll-off factors profile, derived in Section 3.5. Finally, simulation and results are presented in Section 3.6 and the conclusion is in Section 3.7.

3.2 Axis Warping as a Unitary Transformation

Time axis or frequency axis warping [34] can be described as the manipulation of the sampling points of that axis, from equispaced to nonuniformly spaced samples. It is performed by changing of variables or mapping the axis of change from a linear operator to a nonlinear operator, allowing us to smoothly slow the signal at some points and speed it up at other points. Sinc pulses have high side lobes that die slowly, so a big set of apodization functions exists for the purpose of suppressing those sidelobes at the expense of extending the occupancy of pulses in the transform domain. In this study, we will work with Raised Cosine (RC) windowing function. However, the principle should not be limited to this windowing function. In RC pulses, the roll-off factor α is the degree of freedom that suppresses the side lobes of the RC pulse on the expense of extending it in the transform domain. The motivation behind introducing the operation of axis warping is to add an extra degree of freedom to control the time-frequency occupancy compromise.

A signal can be presented in terms of its orthonormal bases, in the Hilbert space of square integrable functions. This space has its inner product defined as $< g, h >= \int g(\tau)h^*(\tau)d\tau$ for $g, h \in L^2$, norm is defined as $\| h \|^2 =< h, h >$. A variety of bases changing transformations can be applied to a signal, converting the traditional coordinate system into a new system with different properties, those are called unitary transformations. A unitary operator U is a linear transformation from a specific Hilbert space onto another $U : L^2 \longmapsto L^2$ [36], as an example, Fourier transform is a unitary transformation that maps the signal from the time axis to the frequency axis. A general formula for representing a unitary

transform U on L^2 for a signal s uses the following integral.

$$(U_s)(\tau) = \int K_U(\tau, v)s(v)dv \tag{3.1}$$

With the integration Kernel K_U is composed of orthonormal sets on L^2.

Axis warping is a subclass of unitary transformations, which can be represented as

$$(U_s)(x) = |w'(x)|^{1/2}s[w(x)] \tag{3.2}$$

Where w the axis warping function, is a smooth monotonic one-to-one function, that sets the relationship between the new time-frequency coordinates and the standard coordinates. Generally warping can be applied to time domain or frequency domain, and it affects the new coordinates according to the following equations.

$$\tilde{x} = w(x) \quad , \quad \tilde{y} = y \ \frac{dw^{-1}(w(x))}{d\tilde{x}}. \tag{3.3}$$

If the warping was on the time axis, x would represent the time operator, and y would represent the frequency operator. If the warping was on frequency axis, x would represent the frequency operator, and y would represent the time operator. As an example, let the warping function on the time axis be $w(t) = (1 - sig(t))\ t + sig(t)\ \frac{1}{2}t$, where $sig(t)$ is a sigmoid function that equals 1 as $t \to \infty$, and equals 0 as $t \to -\infty$. Obviously this warping function smoothly warps the time axis from t to twice its scale $2t$, as if it is smoothly slowing the time axis. As a Unitary transform, the warping should affect the time and frequency lattice in the same time with the relationship in (3.3). Figure 3.1 shows the warping effect on the time-frequency lattice.

In this study, the criterion for generating the warping function is to equalize the spread caused by the roll-off factors of the RC pulses. For windowing in Figure 3.2(a), the window is applied to all the pulses equally. The inner pulses are treated the same as the outer pulses, so the windowing extension for the inner pulses are considered as a waste. On the other hand, the warping replaces the extension to the other domain but only for the outer pulses that have higher roll-off factors α. As shown in Figure 3.2(b), the warping function is supposed to modify the time-frequency lattice to make room for pulses with high α at the

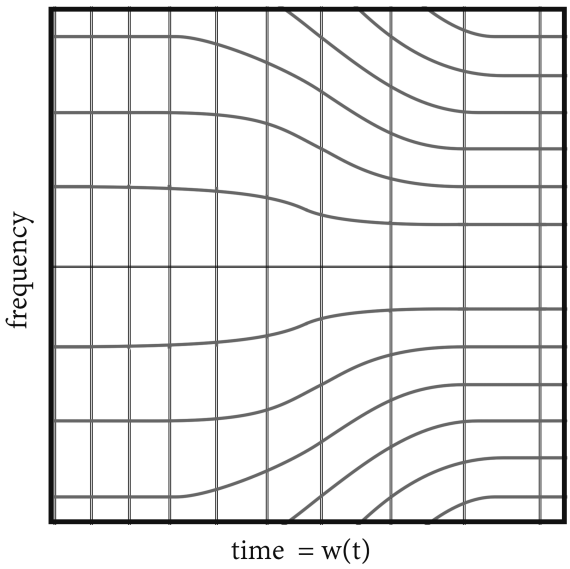

Figure 3.1: warped time-frequency lattice

edges of the signal band, while keeping the window size in the transform domain the same. Hence, keeping the rectangular shape of the signal in the standard time-frequency lattice. Therefore, the warping function should be dependent on the roll-off factor profile. Before discussing the generation of the warping function, we would like to propose the implementation of the warping idea in single carrier systems.

3.3 Time-Axis Warping Implementation

In this section, the implementation of warping the time axis is applied to single carrier systems. The transmitter and the receiver are proposed to use a modified version of Discrete Fourier Spread OFDM (DFT-S-OFDM) [22], as it allows using low complexity frequency domain equalization (FDE) [37]. Briefly, DFT-S-OFDM system takes the modulated data symbols from the time domain to the frequency domain through a DFT process with length M. Then back to time

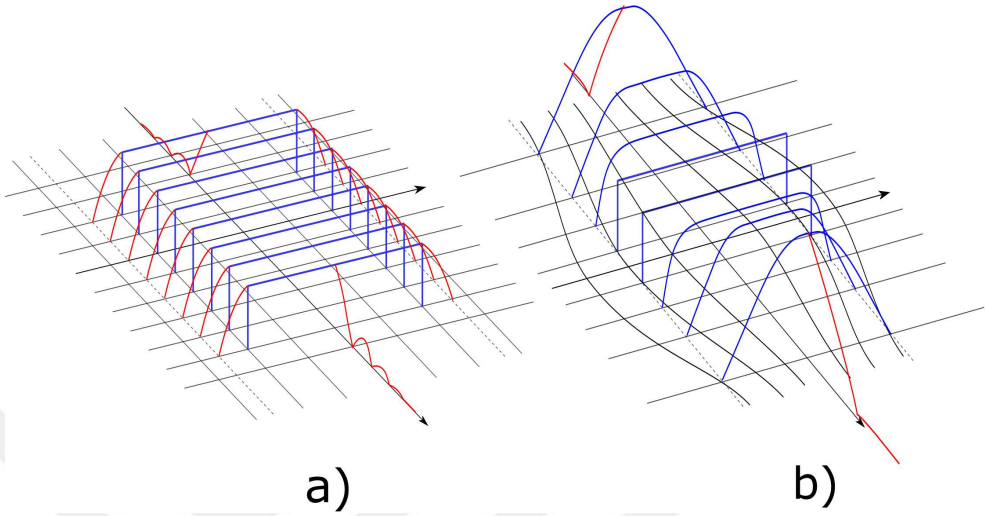

Figure 3.2: Containment in time-frequency space for a) windowed b) Axis warped Signals.

domain through an inverse fast Fourier transform (IFFT) process of a length N higher than the DFT length. This acts as shaping the symbols each into an upsampled sinc shaped pulse, with upsampling ratio N/M. The sinc shape is due to the inherent rectangular shaped window of the DFT and IFFT processes. Note that the axis-warping principle can be applied to any system, and not to be dedicated to the following scheme only.

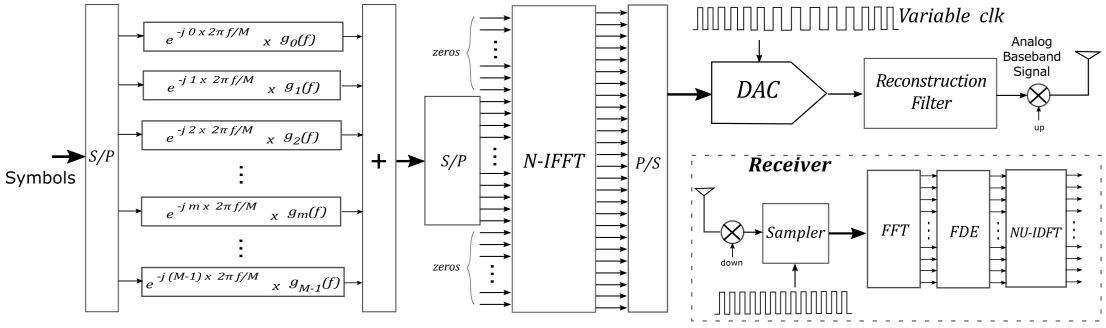

Figure 3.3: Transmitter and receiver implementation

3.3.1 Transmitter Implementation

The DFT process is replaced by a filter bank (FB) process [26] to give the pulses an RC shape with α that varies with the position of the pulse, as done before in [33]. The filter bank is in the frequency domain. Therefore the filter bank branches are RC windowed. The output of the filter bank is

$$B(f) = \sum_{m=0}^{M-1} q(m)\ e^{-jm2\pi f/M} g_m(f) \tag{3.4}$$

where M is the number of the input data symbols, m is the subcarrier increment in the frequency domain, and accordingly the place of the pulse in the time domain, $g_m(f)$ is the RC window shape. Like DFT, f is defined as $f = 0, 1, \cdots, M-1$. So, $g_m(f)$ is also a vector with M samples, and the filter bank block is represented by an $M \times M$ square matrix. For lower computational complexity, filter banks can be implemented using polyphase networks [26]. The output of the filter bank is applied to the IFFT block, and the output word is a circular symbol with different RC shaped pulses:

$$word(n) = IFFT(B_{M\times M} \times P_{M\times N}) \tag{3.5}$$

where n are the time domain samples, $P_{M\times N}$ is the mapping matrix that represents the mapping operation before the N-sized IFFT block, and $N > M$. Due to the roll-off factors profile α_m, that increases near the edges, the edge pulses exceeds the assigned bandwidth for the inner pulses. The warping will squeeze the pulses near the edges in the frequency domain by extending it in the time domain. A variable rate sampler can emulate the effect of time-axis warping. As shown in Figure 3.3, the digital to analog converter (DAC) is triggered via a varying rate clock. After the quantized signal passes through the reconstruction filter, the signal will be time-axis warped, with the warping function $w(n)$ determined by the clock instantaneous rate.

$$warped\ word(t) = word\big(w(n)\big) \tag{3.6}$$

The variable rate clock can be generated by a variable frequency shifter shown in Figure 3.4. The function of this frequency shifter is the delay or the furtherance of

the clock edge, based on the first derivative of the warping function. The theory of frequency synthesis [38] requires multiplying the reference frequency, followed by a frequency division operation. Phase locked loops (PLL) [39] uses the same concept, where the oscillator acts as the multiplier, and a divider or a counter block is applied in the feedback of the loop. In the proposed case there is no need for a loop, as it is already known how the frequency will be manipulated. The reference clock is multiplied by a factor M_{clk} then divided by a factor N_{clk}. This shifts the clock rate from f to fM_{clk}/N_{clk} The division factor decreases to speed up the clock and increases to slow down the clock depending on the warping function requirements. Generating a warping function will be discussed based on the nature of frequency synthesizer systems, after discussing the receiver architecture.

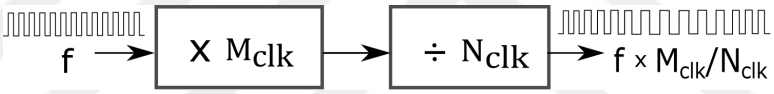

Figure 3.4: Frequency shifter

3.3.2 Receiver Implementation

At the receiver to reduce the complexity of the implementation uniform sampling is performed. As shown in Figure 3.3, the signal gets sampled with an analog to digital converter (ADC), that is driven by a uniform rate clock. The sampled points pass through a fast Fourier transform (FFT) block. The FFT transforms the equispaced time samples to equispaced frequency coefficients. Frequency domain equalization is performed, same as conventional OFDM systems. After the equalization, the original nonuniformly sampled data symbols need to be extracted. An inverse non-uniform discrete Fourier transform (INDFT) should be used to extract the data symbols. It is categorized in the literature [40] as inverse NDFT type 2, which transforms equispaced frequency coefficients to non-equispaced time samples, and not to be confused with NDFT type 4. Which

transforms non-equispaced frequency coefficients to equispaced time samples. Inverse NDFT type 2 can be implemented with low complexity non-iterative algorithms. The direct evaluation technique for INDFT requires a computational complexity of $O(N^2)$ operations. The less complex option is to couple an IFFT operation with an interpolation scheme. That interpolates to the q nearest equispaced points resulting from the IFFT. The complexity of this algorithm is $O(N\ log\ N + Nq)$ operations.

3.4 Generating the Warping Function

Formulating the warping function is necessary for designing the transmitter and the receiver independently. The warping function determines the time-frequency reshaping. In the context of this study it describes the frequency domain shrinkage, hence the extension of time domain, at the region of pulses at the edges of the data stream. The aim behind this is to equalize the effect of high α values on the spectrum occupancy, as mentioned in the previous sections.

For the previously proposed implementation techniques of the transmitter and the receiver, or for any other techniques, the hardware always will have a limitation on the frequency shift resolution. For instance, the position of samples in time for a variable rate frequency synthesizer is bounded by the resolution of the ratio M_{clk}/N_{clk}. Therefore, the time axis is discrete, and the warping function is a piecewise function with discrete intervals bounded by hardware resolution, as shown in Figure 3.5. It shows that the signal sampling points gets shifted by the warping function to new discrete positions. It also shows that the slopes of the warping functions are also discrete.

A drawback from dealing with a warped pulse is that it spans on different slopes of the warping profile, and it has different extension values along the warped axis. Hence, in the frequency domain, it is not fully bounded by abrupt frequency limits, after which the pulse power is zero. This means that there will be a leakage of pulse power out of the dedicated frequency limits. It is also tedious to get a

closed form of the pulse shape in the frequency domain. Therefore, a numerical technique is used to derive the proper warping profile. A good warping profile is the one that changes its slope gradually based on the gradual change of the roll-off factors while maintaining most of the power within a specified frequency window. So the warping function should maximize the following value, with the least slopes of w.

$$C = \sum_{n=1}^{M} \int_{-f_m}^{f_m} DFT[\ P_n(w(t), \alpha_n)\ ]^2\ df \tag{3.7}$$

with C referring to the contained power within the bandwidth $2f_m$. The pulses P_n each has a different α_n. The warping function can be written as

$$w(t) = \begin{cases} s_0 t + d_0 & ; t < m_1 \\ s_1 t + d_1 & ; m_1 < t < m_2 \\ \vdots & \\ s_j t + d_j & ; m_j < t < m_{j+1} \\ \vdots & \end{cases} \quad ; s_j < s_{j+1} \tag{3.8}$$

The warping function is a monotone piecewise function, so the solution involves searching for slopes with the condition of monotonicity. Assuming that the optimum roll off factor is already determined, which will be driven in the next section. The solution of this problem involves searching for the proper slopes of the warping function; that satisfies the maximum containment of the pulses in the frequency domain, or generally speaking, the transform domain. In this section, we propose solving the problem iteratively starting from a specific point. The algorithm to find the proper slopes of the warping function is described below, in Algorithm 2. No matter the point where it starts the algorithm will be the same. First, the frequency limits are set $[-f_m, f_m]$, then the allowed power leakage percentage in the frequency domain to be decided. Then the loop starts by calculating the containment ratio of each pulse r_n

$$r_n = \frac{\int_{-f_m}^{f_m} DFT[\ P_n(w(t), \alpha_n)\ ]^2\ df}{\int_{-\infty}^{\infty} DFT[\ P_n(w(t), \alpha_n)\ ]^2\ df} \tag{3.9}$$

Then the iterations go by increasing the slopes at the pulses needs more containment to reach the specified limit r, and decreasing the local slopes for the pulses

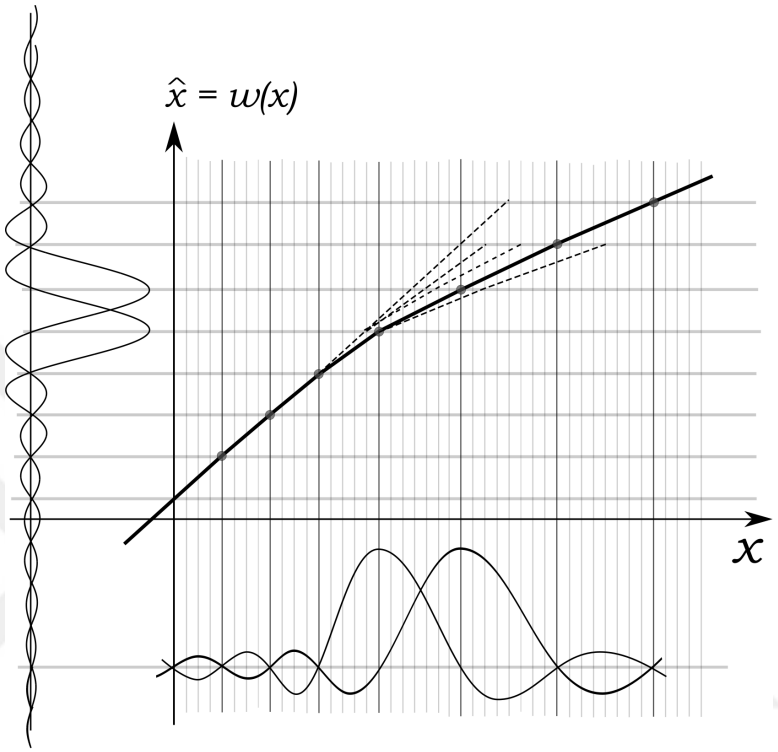

Figure 3.5: Graphical representation of generating the warping function $w(x)$

that are contained more than needed. Finally, the algorithm should converge at the optimum warping function for the given α profile.

This means that the warping function should be dependent on the roll-off factors profile. Therefore, the α values should be chosen to suppress the pulse leakage in the time domain, while at the same time, it does not require much expansion by the warping function. In order to save the spectral efficiency, in the next section, an optimum roll off factors will be derived.

3.5 Roll-off Factors Profile of RC Pulses

Sidelobes of the RC pulses at the edge of the band contributes most of the out-of-band power, and as far as we go away from the edge this contribution gets less. Therefore, it is intuitive to have pulses with high α near the edges, as a high

Algorithm 2 Building a warping function

```
Set   [−f_m , f_m ]
Set   r
Set   w' , s_0 = s_1 = s_2... = 1
loop
    calculate all r_n
    if r_n > r then
        s_n ← s_n − k
    else if r_n < r then
        s_n ← s_n + k
    end if
end loop
```

roll-off factor translates into lower sidelobes. While the pulses away from the edge does not need to have high α values. Let us assume RC pulses in the x domain at the edges of a band, as shown in Figure 3.6. All the side lobes of the pulses add up causing the out of band power. When the first pulse on the edge has a roll-off factor $\alpha_1 = 1$, the sidelobes of this pulse have the highest suppression. To keep the pulse orthogonal with other pulses in the band, and to occupy the same window in the transform domain y, the warping function should extend the x axis with a factor of $(1 + \alpha_1)$ which is 2 for the edge pulse. This extension is a cost that is paid to get side lobes suppression. All the pulses near the edge contribute to the out-of-band power, with different weights, and therefore they should all get their sidelobes suppressed. Consequently, an extension cost will be paid for each of them. This extension adds up at the end, causing a loss in spectral efficiency, hence this expansion must be treated carefully to get the most out-of-band suppression with the least warping expansion.

By moving further from the edge, pulses start to contribute less to the out-of-band power; hence it would be a loss to assign high α values for those pulses. This is exactly a case of Diminishing Marginal Utility [41]. As an economics concept, diminishing marginal utility states that, as we spend more of a factor, which is in our case roll-off factor of the pulses, the marginal utility diminishes. In our case, the out-of-band power reduced contribution for each pulse is what diminishes. Following this analogy, roll-off factors will be chosen according to the law of equalizing marginal utility. Choosing the utility as the suppression of first

out-of-band sidelobe, and the cost of the expansion resulting from the warping function. The law of equalizing marginal utility in our case will translate into; the expansion that is paid for suppressing the second lobe of the second pulse should be the same as the expansion paid for suppressing the first lobe of the first pulse, as shown in Figure 3.6. It goes on like this for the rest of the pulses.

$$\frac{u_1}{c_1} = \frac{u_2}{c_2} = \quad \cdots \quad = \frac{u_n}{c_n} \tag{3.10}$$

There can be different criteria of representing the utility u_n, depending on the system deign requirements. In this study the criterion chosen, is that u_n represents the power suppression of the first side lobe after the band edge, as it has the highest power. Assuming the worst case, when all the pulses side lobes constructively interfere, the total power under the first lobe P_T -as a function of $\tilde{x}$- can be represented as

$$P_T(\tilde{x}) = \big(\ L_1(\tilde{x}) + L_2(\tilde{x}) + \ldots + L_n(\tilde{x})\ \big)^2 \tag{3.11}$$

$L_n(\tilde{x})$ represents the value of the n^{th} lobe of the n^{th} pulse at $\tilde{x}$. The total power under the first lobe is

$$P_T = \int_{1^{st}lobe} \big(\ L_1(\tilde{x}) + L_2(\tilde{x}) + \ldots + L_n(\tilde{x})\ \big)^2 d\tilde{x} \tag{3.12}$$

After, for example, suppressing the first lobe of the first pulse to become L_{s1}, the power difference is represented as the utility u_1 of suppressing the first pulse

$$\begin{aligned} u_1 = \int_{1^{st}lobe} & L_1^2(\tilde{x}) - L_{s1}^2(\tilde{x}) + \\ & 2\big(L_1(\tilde{x}) - L_{s1}(\tilde{x})\big)\ \big(L_2(\tilde{x}) + \ldots + L_n(\tilde{x})\big)\ d\tilde{x} \end{aligned} \tag{3.13}$$

The previous value can be approximated, by the assumption that $L_1^2(\tilde{x}) - L_{s1}^2(\tilde{x})$ are of much lower values than the rest of the integration terms, and they can be dropped. Hence, the utility u_n can be represented with the following approximate proportionality

$$u_n \ \underset{\sim}{\propto}\ \int_{1^{st}lobe} \big(L_n(\tilde{x}) - L_{sn}(\tilde{x})\big) d\tilde{x} \tag{3.14}$$

Where L_{sn} is the value of the n^{th} suppressed lobe of the n^{th} suppressed pulse.

$$u_n \ \underset{\sim}{\propto}\ \int_1^2 sinc(\tilde{x}+n)\left[1 - \left(\frac{cos(\pi\alpha_n(\tilde{x}+n))}{1-(2\alpha_n(\tilde{x}+n))^2}\right)\right] d\tilde{x} \tag{3.15}$$

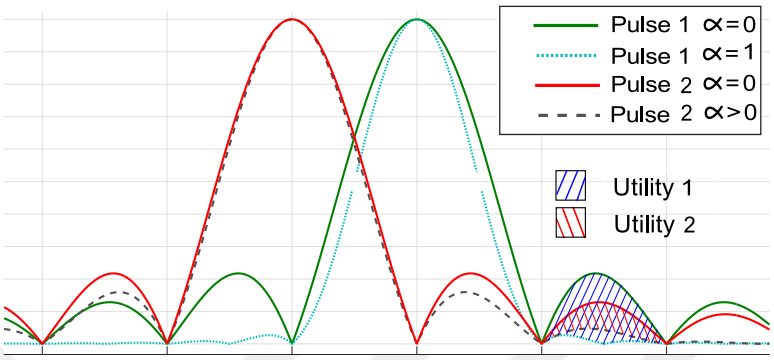

Figure 3.6: Sidelobes suppression as a marginal utility

The warping function will be generated in a way, that the expansion cost c_n spent on each pulse is proportional the roll-off α_n. The warping function will be a smooth interpolating polynomial, while the roll-off factor profile is a discrete function. Therefore, the accurate local expansion resulting from interpolating the warping function is hard to calculate without going through several iterations. For a first order calculations it is assumed that $c_n \propto \alpha_n$. From (3.10), equalizing marginal utility is written as:

$$\begin{aligned} &\frac{1}{\alpha_1}\int_1^2 sinc(\tilde{x})\left[1-\left(\frac{cos(\pi\alpha_1(\tilde{x}))}{1-(2\alpha_1(\tilde{x}))^2}\right)\right]d\tilde{x} = \\ &\frac{1}{\alpha_n}\int_1^2 sinc(\tilde{x}+n)\left[1-\left(\frac{cos(\pi\alpha_n(\tilde{x}+n))}{1-(2\alpha_n(\tilde{x}+n))^2}\right)\right]d\tilde{x} \end{aligned} \tag{3.16}$$

The numerical solution of the equation is presented in the results section. In the simulation and results section, the roll-off factor values are used directly to generate the warping function and to show the gain in signal containment over conventional systems.

3.6 Simulations and Results

In the first part of this section, the driven roll-off factors and warping function will be shown. In the second part, the gain in signal containment in the time domain will be calculated. The power spectral density is shown in the third part.

In the last part, the BER performance of the proposed warped FB-S-OFDM is compared with ZT DFT-S-OFDM, in a time dispersive channel, with exponential and uniform power delay profiles.

3.6.1 Roll-off and Warping Functions

Based on (3.16), the solution of the optimum roll-off factors profile is presented in Table 3.1, with the index n referring to pulse position. Then the α values are used by the algorithm in Section 2.4, to determine the optimum warping function. It is assumed in the calculations that the max resolution of the warped time axis is $T_s/16$, where T_s is the time sampling period. The first derivative result of the warping function w', also the samples spacing in time, are presented in Table 1.

It can be seen that for inner pulses that the α values tend to be zero, while the warping derivative $w' = T_s$. Assuming that N is the max number of data symbols, as the pulse index approach N or 1, the α values increase until it reach 1, and $w' = 2 \times T_s$. The gradient is only over 20 data symbols on each side of the data stream. This is regardless of the length of the stream N. From these results, the total extension caused by warping can be calculated by summing up the sampling durations exceeding T_s. Regardless of N the result is $8.75T$, where T is the data sample duration.

3.6.2 Containment in the Time Domain

In ZT DFT-S-OFDM zeros are inserted in the data stream with a length equivalent to channel maximum delay spread, as an alternative for CP. The non-zero power of the tails leaks to the nearby symbols in the presence of time dispersive channels, which degrades the performance of the system. In this section, the zero tails of the proposed warped signal are compared with the zero tails of ZT DFT-S-OFDM. As shown in Figure 3.7 the gain is calculated in case of the same zero-tail duration length $zt = 10T$, and in the case of having an extra

Table 3.1: The optimum warping and roll-off factor profiles

n	α_n	w'/T_s	n	α_n	w'/T_s
1	1	32/16	N-24		16/16
2	0.6157	28/16	N-23		16/16
3	0.4431	24/16	N-22		16/16
4	0.3458	22/16	N-21		16/16
5	0.2833	21/16	N-20		16/16
6	0.2399	20/16	N-19	0.0799	17/16
7	0.208	19/16	N-18	0.0843	17/16
8	0.183	19/16	N-17	0.0891	17/16
9	0.164	18/16	N-16	0.0945	17/16
10	0.148	18/16	N-15	0.1006	17/16
11	0.136	17/16	N-14	0.107	17/16
12	0.125	17/16	N-13	0.1155	17/16
13	0.1155	17/16	N-12	0.125	17/16
14	0.107	17/16	N-11	0.136	17/16
15	0.1006	17/16	N-10	0.148	18/16
16	0.0945	17/16	N-9	0.164	18/16
17	0.0891	17/16	N-8	0.183	19/16
18	0.0843	17/16	N-7	0.208	19/16
19	0.0799	17/16	N-6	0.2399	20/16
20	0.06	16/16	N-5	0.2833	21/16
21	0.04	16/16	N-4	0.3458	22/16
22		16/16	N-3	0.4431	24/16
23		16/16	N-2	0.6157	28/16
24		16/16	N-1	1	32/16

guard of 5 data symbols for ZT DFT-S-OFDM. Note that the warping function will be shifted from both sides to the positions of the first and last data pulses. So, warping slopes in the zero-tails region are $2T_s$. The gain is calculated as the energy in the zero-tails of ZT DFT-s-OFDM, over the energy in the zero-tails of the time warped signal. The gain over a ZT DFT-s-OFDM with $z_t = 10$ is 12.38 dB. While in the case of putting a guard that compensates for the time extension of the time warped signal $z_t = 15$, the gain is 9.1 dB.

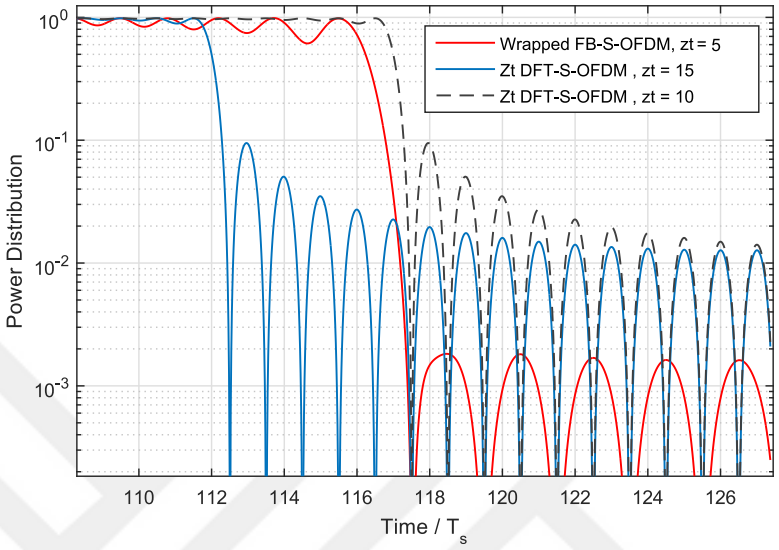

Figure 3.7: Power distribution of zero-tails

3.6.3 Spectral Containment

It is known that ZT DFT-s-OFDM has low OOBE because the symbol starts and ends with low power tails. For the proposed waveform, it can be seen from the power distribution over time that the abrupt transitions at the edges of the symbol are almost eliminated, which reduces the OOBE further. The dominant part of the OOBE of the time warped signal is caused by the transition between different slopes of the warping function, or sampling rates along the time axis. Though, as shown in Figure 3.8, it is still less or comparable to the OOBE of ZT DFT-s-OFDM, without filtration for both waveforms. The figure also shows the OOBE of non-windowed OFDM symbol as a reference.

3.6.4 BER Performance Evaluation

In this section, the system proposed in Section 3.3 is evaluated in a multipath Rayleigh fading channel, with exponentially decaying and uniform PDPs. The rms delay spread of the exponential PDP is $\tau_{rms} = 1.75T$. For the uniform PDP the maximum excess delay is $\tau_{max} = 10T$. Where T is the data sample duration.

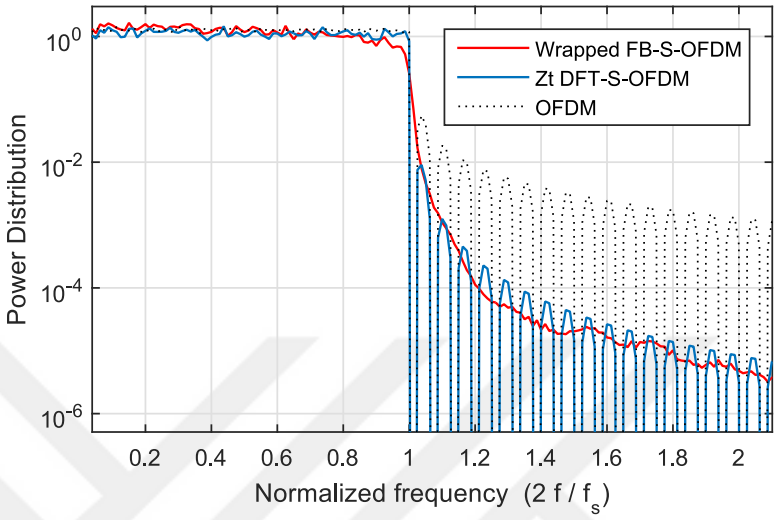

Figure 3.8: Spectral distribution

The interference is simulated with two consecutive QPSK modulated symbols. The zero-tail of the first symbol leaks into the second symbol and degrades its performance. The simulations are based on evaluating the performance of the second symbol, taking the interference into account.

Full channel knowledge at the receiver is assumed, and zero-forcing FDE equalization is performed. Figures 9 and 10, shows the comparison between the warped FB-s-OFDM and ZT DFT-s-OFDM. There are two cases for the ZT DFT-s-OFDM. The first is that it has the same zero tails time duration. The second case adds 9 zero pulses as a guard; that compensates for the loss in spectral efficiency in the warped signal. Hence, the second case is more fair to compare with. It is shown that the conventional ZT DFT-s-OFDM suffers from higher error floor in BER performance because the system performance is inter-symbol interference (ISI) limited. The proposed system shows better performance, even than the case where guard pulses exist, because it exhibits less leakage, consequently less interference and better BER performance. In the presence of an exponential PDP, The warped signal has 3 dB better error floor than a conventional signal of equivalent spectral efficiency. We can also see that, as the channel moves from an exponential PDP to a uniform PDP, the system shows more immunity. The warped signal has 5.5 dB better error floor than the conventional signal of the

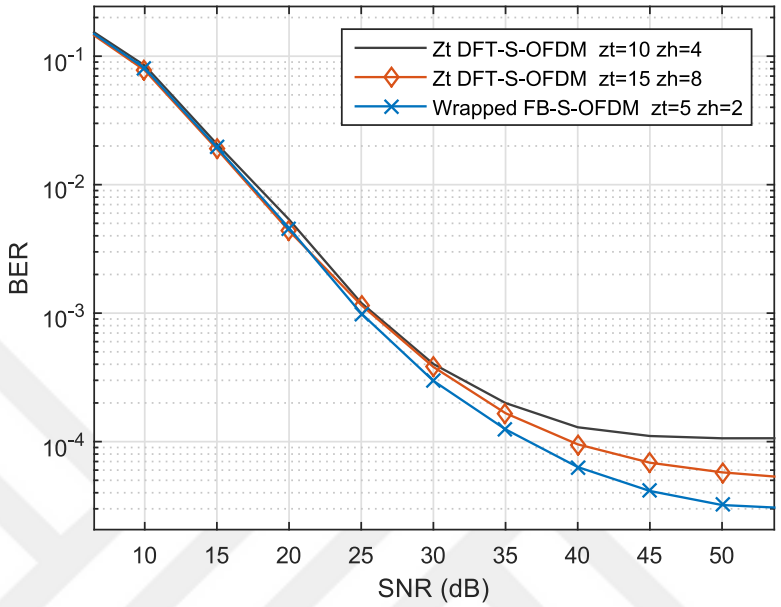

Figure 3.9: BER vs SNR exponential PDP $\tau_{rms} = 1.75T$

same spectral efficiency.

3.7 Conclusion

In this study the idea of applying the time-frequency space warping principle to get well-localized signals is presented. The principle allows mixing pulses that have high sidelobes and high spectral efficiency with pulses that have low sidelobes and low spectral efficiency, all in the same symbol. An implementation technique is proposed that uses raised cosine pulses. Orthogonality was preserved even for a smooth transition between roll-off factors. The transmitter uses a filter bank spread OFDM system, and a variable rate DAC to introduce the warping operation. The receiver uses an inverse non-uniform Fourier transform operation to reverse the warping operation. Also, generating a warping function that depends on roll-off factors has been discussed. An optimum roll-off factors profile has been driven based on the principle of equalizing marginal utility. Simulations show significant improvement in signal containment and BER performance in

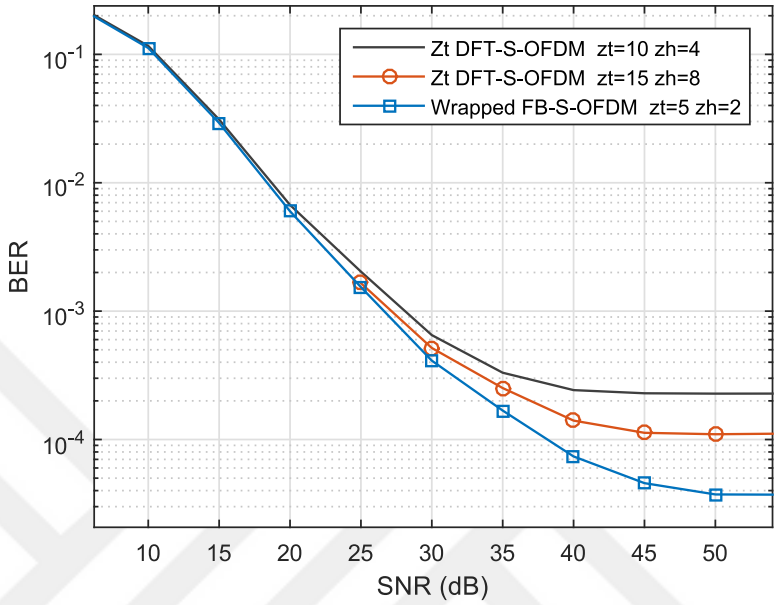

Figure 3.10: BER vs SNR uniform PDP $\tau_{max}10T$

time dispersive channels. The warped signal has a localization gain of 12.3 dB over a conventional signal with the same zero tail duration, and a gain of 9.1 dB over a conventional signal with the same spectral efficiency. Also, the BER gains range from 3 dB to 5.5 dB depending on the channel PDP.

Bibliography

[1] D. W. Matolak, "Air-ground channels & models: Comprehensive review and considerations for unmanned aircraft systems," in *Aerospace Conference, 2012 IEEE*, pp. 1–17, IEEE, 2012.

[2] P. Bello, "Characterization of randomly time-variant linear channels," *Communications Systems, IEEE transactions on*, vol. 11, no. 4, pp. 360–393, 1963.

[3] M. Patzold, *Mobile fading channels*. John Wiley & Sons, Inc., 2003.

[4] T. S. Rappaport *et al.*, *Wireless communications: principles and practice*, vol. 2. Prentice Hall PTR New Jersey, 1996.

[5] E. Haas, "Aeronautical channel modeling," *Vehicular Technology, IEEE Transactions on*, vol. 51, no. 2, pp. 254–264, 2002.

[6] S. M. Elnoubi, "A simplified stochastic model for the aeronautical mobile radio channel," in *Vehicular Technology Conference, 1992, IEEE 42nd*, pp. 960–963, IEEE, 1992.

[7] C. Heller, C. Blumm, and B. Fourestie, "On the characterization of the wireless channel for aeronautic mobile telemetry in c-band," in *Digital Avionics Systems Conference (DASC), 2013 IEEE/AIAA 32nd*, pp. 2D3–1, IEEE, 2013.

[8] D. Cox, "Delay doppler characteristics of multipath propagation at 910 mhz in a suburban mobile radio environment," *Antennas and Propagation, IEEE Transactions on*, vol. 20, no. 5, pp. 625–635, 1972.

[9] G. Acosta, K. Tokuda, and M. A. Ingram, "Measured joint doppler-delay power profiles for vehicle-to-vehicle communications at 2.4 ghz," in *Global Telecommunications Conference, 2004. GLOBECOM'04. IEEE*, vol. 6, pp. 3813–3817, IEEE, 2004.

[10] S. Gligorevic, T. Jost, and M. Walter, "Scatterer based airport surface channel model," in *Digital Avionics Systems Conference, 2009. DASC'09. IEEE/AIAA 28th*, pp. 4–C, IEEE, 2009.

[11] M. Walter and M. Schnell, "The doppler-delay characteristic of the aeronautical scatter channel," in *Vehicular Technology Conference (VTC Fall), 2011 IEEE*, pp. 1–5, IEEE, 2011.

[12] M. Walter, D. Shutin, and U.-C. Fiebig, "Delay-dependent doppler probability density functions for vehicle-to-vehicle scatter channels," *Antennas and Propagation, IEEE Transactions on*, vol. 62, no. 4, pp. 2238–2249, 2014.

[13] M. Walter, D. Shutin, and U.-C. Fiebig, "Joint delay doppler probability density functions for air-to-air channels," *International Journal of Antennas and Propagation*, vol. 2014, 2014.

[14] W. Newhall and J. Reed, "A geometric air-to-ground radio channel model," in *MILCOM 2002. Proceedings*, vol. 1, pp. 632–636, IEEE, 2002.

[15] G. Dyer and T. Gilbert, "Channel sounding measurements in the vhf a/g radio communications channel," *Aeronautical Mobile Communications Panel, document AMCP/WG-D/8-WP/19, Oberpfaffenhofen, Germany*, 1997.

[16] A. Papoulis and S. U. Pillai, *Probability, random variables, and stochastic processes*. Tata McGraw-Hill Education, 2002.

[17] A. Sahin, I. Guvenc, and H. Arslan, "A Survey on Multicarrier Communications: Prototype Filters, Lattice Structures, and Implementation Aspects," *IEEE Communications Surveys & Tutorials*, vol. 16, no. 3, pp. 1312–1338, 2014.

[18] X. Zhang, M. Jia, L. Chen, J. Ma, and J. Qiu, "Filtered-OFDM - Enabler for Flexible Waveform in the 5th Generation Cellular Networks," in *2015*

IEEE Global Communications Conference (GLOBECOM), pp. 1–6, December 2015.

[19] G. Fettweis, M. Krondorf, and S. Bittner, "GFDM - Generalized Frequency Division Multiplexing," in *Vehicular Technology Conference, 2009. VTC Spring 2009. IEEE 69th*, pp. 1–4, April 2009.

[20] V. Vakilian, T. Wild, F. Schaich, S. ten Brink, and J. F. Frigon, "Universal-filtered multi-carrier technique for wireless systems beyond LTE," in *2013 IEEE Globecom Workshops (GC Wkshps)*, pp. 223–228, December 2013.

[21] M. Bellanger, D. Le Ruyet, D. Roviras, M. Terré, J. Nossek, L. Baltar, Q. Bai, D. Waldhauser, M. Renfors, T. Ihalainen, *et al.*, "FBMC Physical Layer: a primer," *PHYDYAS, January*, 2010.

[22] B. E. Priyanto, H. Codina, S. Rene, T. B. Sorensen, and P. Mogensen, "Initial Performance Evaluation of DFT-Spread OFDM Based SC-FDMA for UTRA LTE Uplink," in *2007 IEEE 65th Vehicular Technology Conference - VTC2007-Spring*, pp. 3175–3179, April 2007.

[23] M. Huemer, C. Hofbauer, and J. B. Huber, "The potential of unique words in OFDM," in *the Proceedings of the 15th International OFDM-Workshop*, (Hamburg, Germany), pp. 140–144, September 2010.

[24] G. Berardinelli, F. M. L. Tavares, T. B. Srensen, P. Mogensen, and K. Pajukoski, "Zero-tail DFT-spread-OFDM signals," in *2013 IEEE Globecom Workshops (GC Wkshps)*, pp. 229–234, December 2013.

[25] S. Weinstein and P. Ebert, "Data Transmission by Frequency-Division Multiplexing Using the Discrete Fourier Transform," *IEEE Transactions on Communication Technology*, vol. 19, pp. 628–634, October 1971.

[26] P. P. Vaidyanathan, "Multirate digital filters, filter banks, polyphase networks, and applications: a tutorial," *Proceedings of the IEEE*, vol. 78, pp. 56–93, January 1990.

[27] B. Kim, J. Kim, D. Kim, J. Son, Y. Cho, J. Kim, and B. Park, "Push the Envelope: Design Concepts for Envelope-Tracking Power Amplifiers," *IEEE Microwave Magazine*, vol. 14, pp. 68–81, imsspecialissuemay 2013.

[28] R. v. Nee and R. Prasad, *OFDM for Wireless Multimedia Communications*. Norwood, MA, USA: Artech House, Inc., 1st ed., 2000.

[29] M. S. El-Saadany, A. F. Shalash, and M. Abdallah, "Revisiting active cancellation carriers for shaping the spectrum of ofdm-based cognitive radios," in *Sarnoff Symposium, 2009. SARNOFF '09. IEEE*, pp. 1–5, March 2009.

[30] T. Weiss, J. Hillenbrand, A. Krohn, and F. K. Jondral, "Mutual interference in OFDM-based spectrum pooling systems," in *Vehicular Technology Conference, 2004. VTC 2004-Spring. 2004 IEEE 59th*, vol. 4, pp. 1873–1877, IEEE, 2004.

[31] A. Sahin and H. Arslan, "Edge windowing for OFDM based systems," *IEEE Communications Letters*, vol. 15, no. 11, pp. 1208–1211, 2011.

[32] Z. E. Ankaralı, A. Sahin, and H. Arslan, "Adaptive roll-off factor utilization for fmt-based fbmc burst structures," 2012.

[33] M. Ibrahim and H. Arslan, "Zero Tail Filter Bank Spread OFDM," in *In Press*, IEEE.

[34] R. G. Baraniuk and D. L. Jones, "Shear madness: New orthonormal bases and frames using chirp functions," *Signal Processing, IEEE Transactions on*, vol. 41, no. 12, pp. 3543–3549, 1993.

[35] F. Marvasti, *Nonuniform sampling: theory and practice*. Springer Science & Business Media, 2012.

[36] R. G. Baraniuk and D. L. Jones, "Unitary equivalence: A new twist on signal processing," *Signal Processing, IEEE Transactions on*, vol. 43, no. 10, pp. 2269–2282, 1995.

[37] D. Falconer, S. L. Ariyavisitakul, A. Benyamin-Seeyar, and B. Eidson, "Frequency domain equalization for single-carrier broadband wireless systems," *IEEE Communications Magazine*, vol. 40, pp. 58–66, April 2002.

[38] B.-G. Goldberg, *Digital frequency synthesis demystified*. Newnes, 2000.

[39] F. M. Gardner, *Phaselock techniques*. John Wiley & Sons, 2005.

[40] A. Dutt and V. Rokhlin, "Fast Fourier transforms for nonequispaced data," *SIAM Journal on Scientific computing*, vol. 14, no. 6, pp. 1368–1393, 1993.

[41] A. Mas-Colell, M. D. Whinston, J. R. Green, *et al.*, *Microeconomic theory*, vol. 1. Oxford university press New York, 1995.

Appendix A

Proof of Orthogonality between Sinc Pulses and Raised Cosine $_{\alpha=1}$ Pulses

The orthogonality condition for two pulses S_0 and S_1 is

$$\int_{-\infty}^{\infty} S_0(f)\ S_1^*(f)\ df = 0 \tag{A.1}$$

S_0 is a sinc shaped pulse, represented in frequency domain as

$$S_0(f) = rect(f)e^{-j2\pi f t_0} \tag{A.2}$$

$rect(f)$ is defined on the interval $[{}^{-1}/_{2T}, {}^{1}/_{2T}]$, and t_0 is the position of the sinc shaped pulse in time domain. S_1 is a RC shaped pulses with $\alpha = 1$, twice the time duration of S_0, and twice the spacing nT, where $n = \pm1, \pm2, \pm3, \cdots$

$$S_1(f) = \begin{cases} T\big(1 + cos(2\pi T f)\big)e^{-j2\pi f(t_0+2nT)} & ;|f| \leqslant \dfrac{1}{2T} \\ 0 & ;Otherwise \end{cases} \tag{A.3}$$

$$\int_{-\infty}^{\infty} S_0(f)S_1^*(f)\ df \quad = T\int_{-1/2T}^{1/2T} \big(1 + cos(2\pi T f)\big)e^{j4\pi f nT}\ df \tag{A.4}$$

$$= T \int_{-1/2T}^{1/2T} \big(1 + cos(2\pi T f)\big)\big(cos(4\pi n T f) + j\ sin(4\pi n T f)\big)\ df$$

$$= T \int_{-1/2T}^{1/2T} \big(1 + cos(2\pi T f)\big)\big(cos(4\pi n T f) + 0\big)\ df \tag{A.5}$$

$$= \frac{T}{4\pi}\left[\frac{sin(4\pi n T f)}{n} + \frac{sin(2\pi(2n-1)Tf)}{(2n-1)} + \frac{sin(2\pi(2n+1)Tf)}{(2n+1)}\right]_{-1/2T}^{1/2T} = 0,$$

$$\forall \quad n.$$